

A Study of Active Galactic Nuclei in Low Surface Brightness Galaxies with Sloan Digital Sky Survey Spectroscopy

Lin Mei^{1,2}, Weimin Yuan³ and Xiaobo Dong⁴

Accepted Received

ABSTRACT

Active galactic nuclei (AGN) in low surface brightness galaxies (LSBGs) have received little attention in previous studies. In this paper, we present detailed spectral analysis of 194 LSBGs from the Impey et al. (1996) APM LSBG sample which have been observed spectroscopically by the Sloan Digital Sky Survey Data Release 5 (SDSS DR5). Our elaborate spectral analysis enables us to carry out, for the first time, reliable spectral classification of nuclear activities in LSBGs based on the standard emission line diagnostic diagrams in a rigorous way. Star-forming galaxies are common, as found in about 52% LSBGs. We find, contrary to some of the previous claims, that the fraction of galaxies containing an AGN is significantly lower than that found in nearby normal galaxies of high surface brightness. This is qualitatively in line with the finding of Impey et al. (2001). This result holds true even within each morphological type from Sa to Sc. LSBGs having larger central stellar velocity dispersions, or larger physical sizes, tend to have a higher chance to harbor an AGN. For three AGNs with broad emission lines, the black hole masses estimated from the emission lines are broadly consistent with the well known $M-\sigma_*$ relation established for normal galaxies and AGNs.

Subject headings: galaxies: active — galaxies: fundamental parameters — galaxies: nuclei

1. Introduction

Galaxies with blue central surface brightness significantly fainter than the classical Freeman value of $\mu_0^B=21.65 \text{ mag arcsec}^{-2}$ are commonly referred to as Low Surface Brightness Galaxies (LSBGs). The exact defining criterion of μ_0^B , which is the central surface brightness of a galactic disk

¹National Astronomical Observatories, Chinese Academy of Sciences, 20A Datun Road, Chaoyang District, Beijing 100020, China. E-mail: meilin05@mails.gucas.ac.cn

²Graduate School of the Chinese Academy of Sciences, 19A Yuquan Road, P.O.Box 3908, Beijing 100039, China

³Yunnan Observatory, National Astronomical Observatories, Chinese Academy of Sciences, Phoenix Hill, Kunming, Yunnan Province 650011, China. E-mail: wmy@ynao.ac.cn

⁴Center for Astrophysics, University of Science and Technology of China, Hefei, 230026, China. E-mail: xbdong@ustc.edu.cn

by convention, varies in the literature, though it falls mostly within $\mu_0^B=22.0 - 23.0 \text{ mag arcsec}^{-2}$ (e.g., O’Neil et al 1998; Bell et al 2000). It has been suggested that LSBGs could account for a significant fraction of all galaxies in the Universe (e.g., Freeman 1970; McGaugh et al. 1995), and thus are an important constituent of galaxies. LSBGs show some extremely different properties from high surface brightness galaxies (HSBGs). The typical value of metallicity in LSBGs is one third of the solar metallicity (Impey & Bothun 1997). Observationally, like Malin 1 (Impey & Bothun 1989), a significant number of LSBGs possess diffuse faint disks with little stellar content but substantial amounts of neutral hydrogen gas. The low surface brightnesses indicates low star formation rates (SFRs) in these systems. Indeed, it has been found that the HI surface mass densities in LSBGs are near or below the critical gas surface density for star formation threshold (Kennicutt 1989; van der Hulst et al. 1993; de Blok et al. 1996; Schaye 2004). These extreme properties imply that LSBGs are less evolved compared to HSBGs. Bulge-dominated LSBGs are redder than disk-dominated LSBGs and both can be well described as exponential surface brightness distribution (Beijersbergen et al. 1999). Bulges of LSBGs were found to be metal-poor compared to those hosted by HSBGs (Galaz et al. 2006). Schombert et al. (1990) found that there is no evidence for heavy dust obscuration in LSBGs. However, a recent study of infrared properties of LSBGs using Spitzer data indicated that modest amounts of dust exist in a fraction of LSBGs, although their metallicity and apparent transparency are low (Hinz et al. 2007).

The low surface brightness, comparable to or fainter than the night sky background ($22.5 - 23.0 \text{ mag arcsec}^{-2}$ in the B band), makes the detection of LSBGs difficult. As such, much less optically selected LSBGs samples than normal HSBGs have been cataloged from surveys by ground-based telescopes (e.g., Impey et al. 1996; Monnier Ragaigine et al. 2003). Impey et al. (1996) published a LSBG catalog of 693 LSBGs derived from the Automated Plate Measuring (APM) machine scans of the UK Schmidt Telescope survey plates. A catalog containing 2469 southern-sky LSBGs also from the APM scans of the UK Schmidt photographic plates was given by Morshidi-Esslinger et al (1999).

Unlike HSBGs, which have been the focus of extensive studies in extragalactic astrophysics over many years, nuclear activity in LSBGs has drawn little attention. This may be due partly to lack of large samples of LSBGs. So far, few secured AGNs with reliable detections have been reported in the literature, not mentioning their properties. Potentially, a study of AGNs in LSBGs is as important as in HSBGs for the following reasons. First, it may provide important and complementary clues to uncover the formation and growth of super-massive black holes (SMBH), since LSBGs may have experienced a different route from HSBGs in their formation and evolution. Second, in light of AGN feedback, the evolution and ecology of LSBGs may be affected by the presence of powerful AGNs. Third, a comparison of different host galaxies environments where AGNs reside in, HSBGs and LSBGs, may shed light on the triggering of AGN activity and the dependence of AGN properties on host galaxies.

However, few yet contradicting results have been given in the literature as to the fraction of LSBGs harboring AGNs. When AGN activity was first searched for via optical spectroscopy in small

samples of LSBGs, a surprising result was suggested that LSBGs seem to have a higher fraction of AGNs. Among 10 giant LSBGs, Sprayberry et al. (1995) found 4 Seyfert 1 and 1 Seyfert 2 nuclei, indicating a significantly high AGN fraction. In a sample of 34 giant, HI-rich LSBGs, Schombert (1998) found a high fraction (40 – 50%) of low luminosity AGNs, similar to that in the magnitude-limited local galaxy sample studied by Ho et al. (1997a), which are mostly HSBGs. However, such a high AGN fraction could not be confirmed by Impey et al. (2001, hereafter Impey01) in a spectroscopic study of 250 LSBGs drawn from the Impey et al. (1996) LSBG sample; in contrast, they found an AGN fraction as low as less than 5%.

It should be noted that in essentially all those previous studies, the identification of AGNs was subjected to large uncertainties, due to the following limitations. Firstly, the optical spectra taken were mostly of low spectral resolution (a resolution $\sim 20\text{\AA}$ used in Impey01) and low signal to noise ratio (S/N), and some of narrow wavelength coverage. As such, the line flux measurements were uncertain, especially those close lines suffering from blending. In most studies above, AGNs were identified as having strong low-ionization features ([NII] and [SII]) combined with [OI], unless a broad Balmer line was present, rather than based on the rigorous line flux ratio diagnostic diagrams. The only case where an emission line ratio diagnostic diagram ($[\text{OIII}]/\text{H}\beta - [\text{SII}]/\text{H}\alpha$) was invoked to separate AGNs and HII regions was in Impey01. However, there are considerable uncertainties in the line ratios, especially for $\text{H}\alpha$, which is heavily blended with $[\text{NII}]\lambda\lambda 6548, 6583$. Secondly, no subtraction of starlight spectrum of the host galaxy was performed in those studies, which is important for search of AGN signatures, especially for low luminosity AGNs, as discussed in detail in Ho et al. (1997b). The spectra of host galaxy starlight could affect severely the detection and measurement of emission lines, by making some weak emission line invisible (such as $\text{H}\beta$), or distort the line fluxes, or even spuriously mimic weak broad emission lines.

The Sloan Digital Sky Survey (SDSS, Stoughton et al. (2002)) has acquired high quality optical spectra of a million galaxies over a large portion of the sky (Strauss et al. 2002), some of which could be LSBGs. On the other hand, we have developed an algorithm for successful removal of host galaxy starlight and for accurate emission line spectral fit (see Zhou et al. 2006 for details). These two provide us with an opportunity to revisit the above unsolved question of AGNs in LSBGs, with much better spectral S/N and resolution ($R = 1800 - 2200$), wavelength coverage, and data homogeneity. The high spectral quality of large LSBG samples provided by the SDSS allows us to study not only the AGN demographics, but also, for the first time, the properties of AGNs in LSBGs. This paper presents such a study of nuclear activity in a LSBG sample. We introduce the sample and the data analysis in Section 2. The demographics of nuclear activity in LSBGs are presented in Section 3, followed by a preliminary study of the properties of LSBG AGNs in Section 4. Discussion and a summary of conclusions are given in the last two sections, respectively. A cosmology with $H_0 = 70 \text{ km s}^{-1} \text{ Mpc}^{-1}$, $\Omega_M = 0.3$, and $\Omega_\Lambda = 0.7$ is adopted.

2. APM–SDSS sample and spectral data analysis

2.1. The APM-SDSS sample

In the northern sky, the largest, well-defined optically selected LSBG sample is the catalog compiled by Impey et al. (1996), which was constructed from the Automated Plate Measuring (APM) machine scans of the UK Schmidt Telescope survey plates. It is the most extensive catalog of LSBGs in the northern sky to date, comprising 693 galaxies in the local universe with redshifts < 0.1 selected from a sky region of 786 square degrees centered on the equator. Among them, 513 galaxies have large angular sizes (The major-axis diameter $D \geq 30''$ at the limiting isophote of the APM scans of 26mag arcsec^{-2}) and 180 have small angular sizes ($D < 30''$). Most LSBGs in this catalog have central surface brightness ranging from $\mu_0^B=21.5\text{mag arcsec}^{-2}$ to $26.5\text{mag arcsec}^{-2}$ in the B band. It should be noted that some of the galaxies with μ_0^B at the bright end may not qualify as LSBG when the $\mu_0^B=22.0\text{mag arcsec}^{-2}$ cutoff is applied. However, a significant fraction of these galaxies is still expected to be LSBGs, since the presence of a galactic bulge residing in a low surface brightness (LSB) disk may apparently result in a bright μ_0^B (Beijersbergen et al. 1999).

We searched for spectral data from the SDSS Data Release 5 (DR5) for the LSBGs in the Impey et al. sample. We found that, out of the 693 LSBGs, 194 have SDSS spectra and were classified as galaxies by the SDSS pipeline. They form our sample of study in this paper. Among them, 95 are also in the spectroscopically observed subsample presented by Impey01. Figure 1 shows the distributions of total B -magnitude and μ_0^B for the whole APM sample and the APM-SDSS subsample. It can be seen that the APM-SDSS subsample spans almost the entire ranges of the total magnitude and μ_0^B , though it drops more quickly at the faint end than the parent sample, due to the magnitude limit of the SDSS spectroscopic survey. It also shows that a large fraction of the APM-SDSS subsample has μ_0^B fainter than 22mag arcsec^{-2} , the minimum of the nominal threshold for LSBGs. For the other objects with $\mu_0^B < 22\text{mag arcsec}^{-2}$, some are likely LSBGs with a (dominating) bulge. Therefore the APM-SDSS subsample can be regarded as being composed of mostly LSBGs, with possible inclusion of some intermediate galaxies in between the typical LSBG and HSBG types. For simplicity, we refer to all the sample objects as LSBGs nominally.

2.2. Spectral data analysis

The SDSS spectra have a wavelength coverage from 3800 to 9200 Å with a resolution of $R \sim 1800\text{--}2200$. As was demonstrated by Ho et al. (1997a), the vast majority of the AGN population in the local universe is low luminosity AGN (LLAGN). For LLAGNs, the optical spectra taken through either slits or fibers are dominated by host galaxy starlight. The SDSS spectra were taken through a fiber aperture of $3''$ in diameter (corresponding to 2.9 kpc at a redshift of 0.05), and thus include large amounts of starlight from the host galaxies for the APM-SDSS sample objects. Careful removal of starlight, especially stellar absorption features, is essential for the detection

and measurement of possible nuclear emission lines. For proper modelling of host galaxy starlight spectra, we use the algorithm developed at Center for Astrophysics, University of Science and Technology of China, which is described in detail in Zhou et al. (2006, see also Lu et al. 2006) and is summarized in Appendix A in this paper.

After subtracting modeled stellar spectra and a power-law continuum, the leftover emission line spectra, if any, are fitted using an updated version of the code described in Dong et al (2005), with improvement made for better recovery of weak emission lines. The broad $H\alpha$ and $H\beta$ lines, if present, are hard to separate from nearby narrow lines. As the narrow Balmer lines and the $[\text{N II}]\lambda\lambda 6548, 6583$ doublet have similar profiles to the $[\text{S II}]\lambda\lambda 6716, 6731$ doublet (Filippenko & Sargent 1988; Ho et al. 1997b; Zhou et al. 2006), we use the $[\text{S II}]\lambda\lambda 6716, 6731$ doublet lines as a template to fit narrow lines. If $[\text{S II}]$ is weak, $[\text{O III}]\lambda 5007$ is then used as the template. The $[\text{S II}]$ doublet are assumed to have the same profiles and redshifts; and each is fitted with as many Gaussians as is statistically justified, generally with 1–2 Gaussians. Likewise, the $[\text{O III}]\lambda\lambda 4959, 5007$ doublet are fitted in a similar way. Furthermore, the flux ratio of $\lambda 5007/\lambda 4959$ is fixed to the theoretical value of 3. When a good model of the narrow-line template is achieved, we scale it to fit the narrow Balmer lines and the $[\text{N II}]\lambda\lambda 6548, 6583$ doublet. The flux ratio of the $[\text{N II}]$ doublet $\lambda 6583/\lambda 6548$ is fixed to the theoretical value of 2.96. For the possible broad $H\alpha$ and $H\beta$ lines, we use multiple Gaussians to fit them, as many as is statistically justified. If a broad emission line is detected at $\geq 5\sigma$ confidence level, we regard it as genuine. If the broad $H\beta$ line is too weak to achieve a reliable fit, we then re-fit it assuming that it has the same profile and redshift as the broad $H\alpha$ line.

Our analysis results in detections of 131 emission line galaxies out of the total 194 LSBGs. This gives a fraction of 68% of emission line galaxies in LSBGs. The objects are list in Table 1, along with the fitted parameters of the important lines. Also listed are the stellar velocity dispersions in the central region of the host galaxies, σ_* , which are obtained in the above procedure of modeling the host galaxy starlight spectra. Three out of the 131 galaxies are found to show broad Balmer emission lines and should be broad line AGNs. Their spectra are shown in Figure 2 and the parameters of the broad lines are given in Table 2. It should be noted that the widths of emission line are corrected for the instrumental broadening, which is 55-80 km s^{-1} for SDSS spectra.

To demonstrate the reliability of our spectral analysis, as well as the spectral quality of the SDSS, we compare our detections of broad line AGNs with those in Impey01. Among the 95 overlapping objects in both the Impey01 spectroscopic subsample and our APM-SDSS subsample, two were claimed to have broad emission lines by the authors. 1226+0105 (SDSS J122912.9+004903.7) is also found in our work with the full width at half maximum (FWHM) of $H\alpha$ 4750 km s^{-1} , which is slightly broader than the previous value (4570 km s^{-1} , Impey01). The narrower FWHM value in Impey01 is likely due to the fact that broad and narrow component deblending could not be performed given the low spectral resolution (20 \AA). For the second object, 1436+0119 (SDSS J143846.3+010657.7), however, we cannot confirm the presence of a broad $H\alpha$ line with the starlight subtracted SDSS spectrum (Figure 3). An inspection of the original spectrum in Impey01 seems

to suggest that the previously claimed broad $H\alpha$ line is likely spurious and just a feature in the stellar spectrum (no starlight subtraction was performed in Impey01) when the resolution and S/N is low. Furthermore, the one with the weakest broad line among the above 3 broad line AGNs in our work (see Figure 2), SDSS J231815.7+001540.2 (NGC 7589), was missed in Impey01. This object is likely a Seyfert 1.9, which was previously found to show strong, highly variable hard X-ray emission (Yuan et al. 2004). We thus conclude that our spectral analysis results are much more accurate and reliable.

It is worth noting that the three LSBGs, J005342.7–010506.6, J111549.4+005137.5 and J133032.0–003613.5 that were classified as type 1 AGNs by Hao et al. (2005), do not show evident broad emission lines in this work. This is likely due to the difference in subtraction of narrow lines. Hao et al. (2005) modeled every narrow line with one single Gaussian. Yet we noticed that the profiles of narrow lines are asymmetric and thus we used 2 Gaussians to model each of the [SII] doublet; the fit is used as a model to subtract the narrow component of $H\alpha$ and [NII], as described in section 2.2. The asymmetric profiles of the narrow $H\alpha$ and [NII] components can mimic a broad $H\alpha$ component (see also Ho et al. 1997b; Greene & Ho 2007). To be conservative, we do not consider these 3 LSBGs as broad line AGNs in this paper.

2.3. Spectral classification of nuclear Activity

Generally, there are three types of emission line spectra in galactic nuclei: star-forming (HII) nuclei in which line emitting gas is photoionized by radiation from hot stars, Seyfert nuclei characteristic of photoionization by a power-law continuum powered by black hole accretion, and Low-Ionization Nuclear Emission Regions (LINERs, Heckman 1980) with relatively strong low ionization lines (such as [OI] λ 6300 and [NII] $\lambda\lambda$ 6548,6583) and generally lower nuclear luminosities compared to Seyfert galaxies. The nature of LINER is still controversial, though an accretion-powered AGN appears to be preferred in recent studies (see, e.g. Ho et al. 1997a). Following Ho et al., we regard LINERs as a subclass of AGN in this paper.

Classification of galactic nuclei based on optical emission lines has been extensively investigated by various authors. One common and effective method is to compare the flux ratios of close lines with predictions of different photoionization models. It was first shown by Baldwin, Phillips & Terlevich (1981, hereafter BPT) that AGNs could be separated from HII nucleus on the diagrams of the line flux ratios [NII] λ 6583 / $H\alpha$ vs. [OIII] λ 5007 / $H\beta$, [OII] λ 3727 / [OIII] λ 5007 vs. [OIII] λ 5007 / $H\beta$, and [OI] λ 6300 / $H\alpha$ vs. [OIII] λ 5007 / $H\beta$ (the BPT diagrams). Veilleux & Osterbrock (1987) revised this method by including the line ratio [SII] $\lambda\lambda$ 6717,6731/ $H\alpha$ and excluding the [OII] λ 3727/[OIII] λ 5007 because it is sensitive to reddening. A similar scheme was also used by Ho et al. (1997b). Using a large sample of SDSS emission line galaxies, Kauffmann et al. (2003, hereafter, Ka03) found a clear, empirical separation between star-forming galaxies and AGNs on the BPT diagram of [NII] λ 6583/ $H\alpha$ versus [OIII] λ 5007/ $H\beta$. This classification scheme was refined recently by Kewley et al. (2006, hereafter, Ke06), by including new criteria to separate

Seyferts from LINERs using the $[SII]\lambda\lambda 6717,6731/H\alpha$ and $[OI]\lambda 6300/H\alpha$ line ratios. In this scheme, galaxies falling in between the empirical star-forming and AGN dividing line of Ka03 and the theoretical limit (maximum star-formation) of Kewley et al. (2001, hereafter, Ke01) are regarded as composite objects (also referred to as transition objects), which likely contain a metal-rich stellar population plus an AGN, either a Seyfert or a LINER (Ho et al. 1997a; Ke06) In this paper, we adopt the classification scheme of Ke06, since it is the most recent updates and also easy to use. Our careful deblending of the [NII] and [SII] doublets ensure that our spectral classification based on these criteria should be reliable.

The classification scheme of Ke06 is summarized here. First, star-forming galaxies are separated from AGNs using the Ka03 dividing line in the $[NII]\lambda 6583/H\alpha$ versus $[OIII]\lambda 5007/H\beta$ diagram: star-forming galaxies are those falling below and to the left-hand side of the dividing line, i.e.

$$\log([OIII]/H\beta) > 0.61/\{\log([NII]/H\alpha) - 0.05\} + 1.3, \quad (1)$$

and AGNs are those falling above and to the right-hand side of the dividing line, i.e.

$$\log([OIII]/H\beta) < 0.61/\{\log([NII]/H\alpha) - 0.05\} + 1.3. \quad (2)$$

AGNs are further grouped into 3 subclasses: composite galaxies are those falling in between the Ka03 and Ke01 dividing lines in the $[NII]\lambda 6583/H\alpha$ – $[OIII]\lambda 5007/H\beta$ diagram:

$$\log([OIII]/H\beta) > 0.61/\{\log([NII]/H\alpha) - 0.05\} + 1.3 \quad (3)$$

and

$$\log([OIII]/H\beta) < 0.61/\{\log([NII]/H\alpha) - 0.47\} + 1.19 \quad (4)$$

Objects falling above the Ke01 maximum starformation line are Seyfert galaxies or LINERs, i.e.

$$\log([OIII]/H\beta) > 0.61/\{\log([NII]/H\alpha) - 0.47\} + 1.19. \quad (5)$$

These two types are further separated in the diagrams of $[SII]\lambda\lambda 6717,6731/H\alpha$ – $[OIII]\lambda 5007/H\beta$ or $[OI]\lambda 6300/H\alpha$ – $[OIII]\lambda 5007/H\beta$, i.e. for Seyfert galaxies,

$$1.89 \log([SII]/H\alpha) + 0.76 < \log([OIII]/H\beta) \quad (6)$$

or

$$1.18 \log([OI]/H\alpha) + 1.30 < \log([OIII]/H\beta); \quad (7)$$

and for LINERs

$$1.89 \log([SII]/H\alpha) + 0.76 > \log([OIII]/H\beta) \quad (8)$$

or

$$1.18 \log([OI]/H\alpha) + 1.30 > \log([OIII]/H\beta). \quad (9)$$

The 131 LSB emission-line galaxies are plotted in the $[\text{NII}] \lambda 6583/\text{H}\alpha$ – $[\text{OIII}] \lambda 5007/\text{H}\beta$ diagram in Figure 5 (upper panel), which are marked by different symbols for different categories. It can be seen that the objects reproduce well the ‘butterfly’-shaped distribution as shown in Ka03, though with much less objects. The star-forming galaxies (crosses) trace well the Ka03 dividing line, spreading over a large range of metallicity. Further separation between Seyferts and LINERs is demonstrated in Figure 5, in which the line ratios $[\text{SII}] \lambda \lambda 6717, 6731/\text{H}\alpha$ – $[\text{OIII}] \lambda 5007/\text{H}\beta$ (middle panel) and $[\text{OI}] \lambda 6300/\text{H}\alpha$ – $[\text{OIII}] \lambda 5007/\text{H}\beta$ (lower panel) are plotted for those with the lines detected with $S/N > 3$. For the objects with both the $[\text{SII}]$ and $[\text{OI}]$ lines detected with $S/N > 3$, these two criteria give mutually consistent classification. Among the three broad line AGN (marked as a filled squares) found in the APM-SDSS sample, two have the narrow line properties as Seyferts and one as composite objects. The resulting classification of each emission line LSBG is given in Table 1. We also overplot in Figure 1 the distributions of the total B magnitudes and μ_0^B for the emission line LSBGs. As demonstrations, in Figure 4 we show example spectra and results of spectral analysis for each of the 3 spectral types. We also list in Table 3 the host galaxy properties of the objects classified as an AGN (Seyfert + LINER + composite), as given in Impey et al. (1996).

3. Demographics of nuclear activity in LSBGs

Of the 194 LSBGs, there are 131 ($68\% \pm 3\%$) showing emission lines. Among them, 101 ($52\% \pm 3\%$) objects are classified as star-forming galaxies and 30 as AGNs ($15\% \pm 2\%$; 6 Seyferts, 12 LINERs, and 12 composite galaxies). The fraction of broad line AGNs is $2\% \pm 1\%$ among LSBGs. This result indicates that the fraction of AGNs is significantly lower than that ($>40\%$) found for the local bright galaxy sample of Ho et al. (1997a), which is predominantly HSBG. The fraction of AGNs is even lower if not all LINERs and composite objects are AGNs.

As discussed in the sample selection above, probably not all the 194 LSBGs are low surface brightness in a strict sense. In fact, 79 (40%) of the 194 LSBGs have μ_0^B from Impey et al. (1996) brighter than $22.0 \text{ mag arcsec}^{-2}$, which are either LSBGs with (dominating) galactic bulges or simply HSBGs. Among them, there are 25 AGNs, yielding an AGN fraction of 31%. Considering possible contamination of HSBGs in this bright subsample, this fraction is likely overestimated and the actual fraction for genuine LSBGs is likely even lower. The remaining 115 galaxies with $\mu_0^B > 22.0 \text{ mag arcsec}^{-2}$ should be mostly bona fide LSBGs (Impey01). Among them, there are only 5 AGNs, making a fraction as low as $4\% \pm 2\%$. This strengthens the above result that LSBGs have a much lower AGN fraction compared to HSBGs.

The incidence of an AGN has been found to be dependent on the Hubble type of a galaxy, that is higher in early type (E–Sb) than in late type galaxies (Ho, et al. 1997a). Since a LSBG sample has a very different Hubble type distribution from HSBGs (the former tends to consist of more late type than the latter), the above result may be a reflection of the incidence of AGNs on galaxy morphology. To investigate this possibility, we calculate the fraction of both AGNs and star-forming galaxies in each morphological type, using the Hubble type information provided in

Impey et al. (1996). The distribution of the objects of each category and their detection rates over the morphological type are shown in Figure.6 (open histograms). Also plotted are the same distributions for the $\mu_0^B > 22.0 \text{ mag arcsec}^{-2}$ subsample (hatched histograms). The numbers are also given in Table 4. It can be seen that the LSBGs have most morphological types later than Sb and peak at Sc, as expected. The detection rate of AGNs is no more than 20% in LSBs of type Sa, Sb, and Sc, and starts to drop to less than 10% in types later than Sc. This result indicates that the overall low AGN fraction of LSBGs than that of HSBGs is real, rather than a consequence that LSBGs tend to have more of later Hubble types, which have in general low AGN fractions, as known previously. Interestingly, it increases up to 50% in interacting galaxies. When galaxies with $\mu_0^B > 22.0 \text{ mag arcsec}^{-2}$ are considered only, the detection rates are even lower, though the sample is small.

3.1. Comparison with HSBGs

Strictly speaking, an appropriate comparison of AGN detection rate between two samples requires that they should have the same redshift (distance) distributions, and have the same spectral data quality and analysis procedures. To make sure that our above results are not significantly affected by those biases introduced in sample selection and observation, we construct a comparing sample of HSBGs with SDSS spectra. The sample is drawn from the Third Reference Catalogue of Bright Galaxies (RC3) (de Vaucouleurs et al. 1991)—a catalog of typical HSBGs—in such a way that it has the same redshift (distance) distribution as that of the APM-SDSS LSBG sample below $z = 0.04$ ¹. This results in a comparing sample consisting of 142 HSBGs with SDSS spectra. For a comparison, the redshift distribution of the HSBG sample is plotted in Figure 7 (middle panel), which is indistinguishable from that of the LSBGs in the $z = 0 - 0.04$ range (the K-S test gives a chance probability of 0.1 that the two distributions are drawn from the same population). The HSBG sample is systematically brighter than the LSBG one in total magnitude, as expected. The SDSS spectra of the 142 HSBGs are analyzed using the exactly same procedure as for the LSBGs in Section 2., ensuring the homogeneity in data analysis.

We compare the LSBG and HSBG samples in the range of $z < 0.04$, and only those with the morphological types of Sa, Sb, and Sc are considered in order to have sufficient objects to ensure statistically meaningful results. The detection rates of AGNs and star-forming galaxies for both the LSBGs and HSBGs are shown in Figure 8. The results for HSBGs (right-hand side panels) are broadly consistent with those obtained by Ho et al. (1997a), suggesting that our results are reliable. Comparisons between the LSBGs (left-hand side panels) and HSBGs show clearly that LSBGs indeed have a low AGN fraction (10–20%) than HSBGs (40–50%), regardless their morphological types. The numbers are also given in Table 5. Thus our above results are confirmed.

¹This redshift cutoff is introduced because there are few RC3 galaxies with $z > 0.04$

Interestingly, the fraction of star-forming galaxies in the LSBGs seems to be comparable to, or even slightly higher than, that in the HSBGs. A surprising difference is found in the distribution of the fraction of star-forming galaxies: in HSBGs, this fraction drops significantly from Sc to earlier types and is the lowest for Sa. While in LSBGs, it keeps a high fraction toward early types and even possible rises for the Sa type.

Summarizing, our results do not apparently support the high AGN fraction reported in Sprayberry et al. (1995) and Schombert (1998), but are consistent qualitatively with that of Impey01.

4. Properties of AGNs in LSBGs

4.1. Power of AGN

Figure 9 shows the distributions of the $H\alpha$ and [OIII] emission line luminosities of the APM-SDSS LSBG sample. The majority of the AGNs have $H\alpha$ luminosities lower than 10^{40} ergs s^{-1} , with a median of 7.5×10^{39} ergs s^{-1} . All of the AGNs in LSBGs have $L[\text{OIII}] < 10^{41}$ ergs s^{-1} and the distribution peaks between 10^{38} – 10^{39} ergs s^{-1} . These values are 2 to 3 orders of magnitude smaller than those of luminous AGN. It has been suggested that the luminosity of the [OIII] λ 5007 line can be regarded as a tracer of AGN activity (Ka03). Therefore, the AGNs in LSBGs are mainly of low luminosity. Interestingly, as inferred from Figure.9, the AGN detection rate becomes higher with higher $L[\text{OIII}]$, i.e. increasing gradually from $\sim 7\%$ at 10^{37} ergs s^{-1} up to $\sim 78\%$ at 10^{41} ergs s^{-1} .

4.2. Properties of emission line region

4.2.1. Narrow line width and stellar velocity dispersion

In AGNs of normal HSBGs, it has been suggested that kinematics of the narrow line region traces well the galactic bulge potential, via the establishment of a tight correlation between the width of the narrow emission lines and the stellar velocity dispersion σ_* . Here we test this relationship for AGNs in LSBGs. The value of σ_* can be obtained in our modeling of the stellar spectra of the host galaxy starlight (Section 2). For 34 LSBGs (19 AGNs and 15 star-forming galaxies) with both σ_* and the [NII] doublet detected at the $> 5\sigma$ level, the relation between σ_* and the [NII] line width is plotted in Figure 10. Strong correlations are found (For AGNs, $\sigma_* = 0.9 \times (\sigma[\text{NII}] - 150.0) + 155.3$; for the whole objects, $\sigma_* = 0.97 \times (\sigma[\text{NII}] - 150.0) + 151.4$. The Spearman correlation test gives a chance probability of 8.6×10^{-6} for AGNs only and 1.5×10^{-9} for AGNs and star-forming galaxies.) Thus, the width of the narrow line $\sigma[\text{NII}]$ traces well the stellar velocity dispersion in LSBGs.

4.2.2. Electron density in the narrow line region

Since in the course of our spectral analysis the [SII] $\lambda\lambda 6717, 6731$ doublet is deblended, we can assess the electron density in the narrow line region (NLR) from the flux ratio of these two lines (e.g., Osterbrock & Ferland 2006; Xu et al 2007). We assume an electron temperature of $T_e = 10^4$ K, a typical temperature of the ionized gas in the NLR of AGNs. The electron densities of AGN in both the LSBG and HSBG sample are estimated, whose distributions are shown in Figure.11. For those with [SII] $\lambda 6717$ /[SII] $\lambda 6731$ flux ratios greater than 1.42, an upper limit of the electron densities is set to be 10 cm^{-3} . A comparison shows that these two distributions are significantly different (a chance probability of 7×10^{-5} given by the K-S test), in a way that AGNs in LSBGs on have average lower NLR electron density than AGNs in HSBGs.

4.2.3. Dust extinction

We examine optical extinction in the emission line nuclei of the LSBGs by assuming that the Balmer decrements in excess of the intrinsic value 2.85 for HII region and 3.1 for AGNs (Veilleux & Osterbrock 1987), are caused by dust extinction. The narrow lines Balmer decrements are calculated for star-forming galaxies and AGNs for both the LSBGs and the HSBGs. For the LSBGs, the median Balmer decrement is 3.3 for star-forming nuclei and 4.0 for AGNs, which correspond to an extinction color excess $E_{B-V} = 0.16$ and 0.24, respectively. For the HSBG comparing sample, the median values are 4.2 for star-forming nuclei and 4.7 for AGNs, which correspond to $E_{B-V} = 0.37$ and 0.40, respectively. This indicates that dust extinction in LSBGs is relatively weaker compared to that in normal galaxies, for both AGNs and star-forming nuclei. A comparison of the distributions of the Balmer decrement between the HSBGs and the LSBGs shows that they are statistically different, for both AGNs and star-forming nuclei (a chance probability of 2.7×10^{-7} given by the K-S test for AGNs and star-forming galaxies).

4.3. Radio and X-ray detectability of AGNs in LSBGs

Observationally, AGNs emit their power over a wide range of frequencies, from radio, optical, to X-rays or even γ -rays. Among the 30 LSBG AGNs, only one, J231815.7+001540.2 (NGC 7589) was detected in X-rays with XMM-Newton, which exhibits large amplitude variability (Yuan et al. 2004). For the other AGNs, the X-ray flux limits set by the ROSAT All-Sky Survey are comfortably consistent with the distribution of the optical-to-X-ray effective spectral indices α_{ox} found for AGNs. Deeper X-ray observations are needed to detect more such AGNs in X-rays.

Of the 30 AGNs in LSBGs, 8 ($26\% \pm 8\%$) were detected by the FIRST (Faint Images of the Radio Sky at 20 cm) survey (Becker et al. 1995), including one with broad emission lines. Among them, 2 are resolved in their radio images. We calculate the radio loudness R, defined as the flux

ratio between 1.4 GHz and the optical B-band. Six objects have $R > 10$ and can be classified as radio-loud. Most of the radio-loud objects of our LSBG AGNs are actually radio-intermediate ($R < 100$), and there is no very radio loud ($R \geq 100$) AGNs. They are all weak radio sources, with 1.4GHz fluxes less than 10 mJy. For the remaining 22 AGNs, 20 were in the FIRST survey field. Assuming an upper flux limit of 1 mJy for the FIRST survey, we found that at least 13 are "radio-quiet" ($R \leq 10$). This makes the fraction of radio-loud fraction as 20%–35%,

5. Discussion

5.1. AGN fraction in LSBGs

We have shown that LSBGs have a lower AGN detection rate compared to HSBGs in the local Universe. The overall fraction of AGNs in the APM-SDSS LSBG sample is $\sim 15\%$. Considering that the APM LSBG sample have possible contamination of some HSBGs, the AGN fraction in genuine LSBGs can be even lower. This result holds true within each of the Hubble types from Sa to Sc. We argue that this result is not caused by any selection effects or detecting biases in observations, since it is confirmed by comparisons with the carefully chosen HSBG comparing sample. In fact, AGNs in LSBGs should be more easy to detect spectroscopically compared to those in HSBGs, since the dilution of AGN spectral features by host galaxy starlight spectra is less severe in LSBGs than in HSBGs. To check whether we have missed a substantial amount of AGNs at larger distances, we examine how the AGN detection rate varies with increasing distances. We find that the AGN detection rate keeps nearly a constant at all distances within the largest redshift of th sample ($z < 0.1$), and thus there is no significant number of faint AGNs missing at large distances.

In general, a low AGN occurrence rate may be possibly due to the inefficiency of fueling gas into the central black holes in galaxies. However, the underlying physical processes responsible for the fueling efficiency is unknown, which is one of the fundamental questions in AGN research. One speculation is that gas in LSBGs may have relative large angular momentum (Dalcanton et al. 1997), even in the inner disk. Alternatively, it may well be possible that this result is just a manifestation of the more fundamental differences between HSBGs and LSBGs in some of the physical properties in the central region of galaxies (such as bulges), which are more directly linked to the onset of nuclear activity.

Motivated by this hypothesis, we search for other potential dependence of the AGN occurrence rate in the LSBG sample. One such dependence is on the physical size of galaxies. Figure 12 shows the distribution of the size of galaxies in the APM-SDSS LSBG sample and the dependence of the AGN fraction on the galaxy scale. The physical scales of the LSBGs are estimated using the angular sizes measured in the SDSS imaging survey by the SDSS pipeline. As can be seen, there exists a clear trend that larger galaxies tend to have a higher fraction of AGNs. This implies that the overall AGN fraction for a sample of LSBGs depends on the distribution of the physical scales

of galaxies in the sample. For the current APM-SDSS LSBG sample, the vast majority of the member galaxies are smaller than 50 kpc, which have very low fractions of AGNs. This finding also implies that, when AGN fractions are compared between two LSBG samples, the distributions of the physical scales have to be taken into account.

Schombert (1998) reported a high occurrence of AGNs ($\sim 50\%$) in his LSBG sample, which are mostly late-type, HI-massive, and large-size galaxies. In fact, using the data presented in Schombert (1998), we also find a similar strong dependence of the AGN fraction on galaxy size. We compare the distributions of galactic sizes between the Schombert (1998) sample and the APM-SDSS sample; however, no significant difference is found (the K-S test gives a probability of 68%). Thus, we anticipate that the higher AGN fraction found in Schombert (1998) than ours is perhaps due to the small sample size, as well as possibly to the relatively coarse spectral quality, and less rigorous spectral analysis and classification method employed.

A similar trend of increasing AGN fraction with the increase of the size of a galaxy is also found for HSBGs in the comparing sample. Meanwhile, we also find that the HSBG sample has relatively systematically larger galaxies in size (with a median of 42.1 kpc) than the LSBG sample (with a median of 37.4 kpc for $z < 0.04$); the K-S test shows that the two distributions are significantly different (a probability level 10^{-5}). As such, the observed lower AGN fraction in LSBGs than that in HSBGs in our study is likely a manifestation of the postulation that LSBGs are systematically smaller in size compared to HSBGs, if the proposed AGN dependence on the physical scale of galaxies is the case. However, these postulations need further confirmation in future studies.

We also test the possible dependence of AGN fraction on galactic bulge properties. It has been found that stellar velocity dispersion σ_* is well correlated with the bulge mass and luminosity, and is thus a tracer of the gravitational potential of the bulge. Given the spectral resolution of SDSS data, the minimum values of σ_* can be measured are around 70 km s^{-1} . For those objects without measurable σ_* , we assume their σ_* to be less than 70 km s^{-1} . Figure 13 shows the distribution of σ_* for the APM-SDSS LSBG sample and for their AGNs, as well as the AGN fraction. It can be seen clearly that the AGN fraction increases in higher σ_* bins. Similar trend is also found in the HSBG comparing sample, which is a known property that AGNs tend to be found in early type galaxies, where bulges are dominant. Our result in Section 3 shows that even for the same Hubble type (Sa–Sc), LSBGs have a lower AGN fraction than HSBGs. In the context of the AGN fraction dependence on bulge properties, this may imply that within a given morphological type, LSBGs have either relatively smaller bulge mass or lower fraction of galaxies with bulges, compared to HSBGs. Again, this postulation needs confirmation by future studies. The dependence of AGN fraction on both the size of galaxies and galactic bulge property is not surprising, since galaxy sizes and σ_* are strongly coupled in the samples studied here. However, we consider the latter relation is perhaps more fundamental, since it has becoming known that the growth of galactic bulges and the growth of central black hole are somehow related (Ferrarese & Merritt 2000; Gebhardt et al. 2000).

5.2. Black hole growth in LSBGs

The broad $H\alpha$ emission lines are well detected in 3 LSBGs. We estimate the masses of central black holes using the linewidth-luminosity mass scaling relation given in Greene & Ho (2007). The values are $2.8 \times 10^6 M_{\odot}$ for SDSS J011448.7–002946.1, $2.0 \times 10^7 M_{\odot}$ for SDSS J122912.9+004903.7 and $3.4 \times 10^6 M_{\odot}$ for SDSS J231815.7+001540.2 respectively. For the two AGNs, SDSS J011448.7–002946.1 and SDSS J122912.9+004903.7, broad components of $H\beta$ are also detected with reliable confidence. It is claimed by Vestergaard & Peterson (2006) that the absolute uncertainties in masses estimated by these mass scaling relationships are about a factor of 4. According to the scaling relationships calibrated by Vestergaard & Peterson (2006) based upon the broad $H\beta$ luminosity, black hole masses are estimated to be $3.6 \times 10^6 M_{\odot}$ for SDSS J011448.7–002946.1 and $4.4 \times 10^7 M_{\odot}$ for SDSS J122912.9+004903.7 are found, respectively.

For these 3 AGN with central black hole mass estimates, the stellar velocity dispersion σ_* can also be measured in our spectral analysis. We are therefore able to, for the first time, test the relationship between black hole mass and stellar velocity dispersion ($M-\sigma_*$) relation for LSBGs, though the number of objects is very small. The result is shown in Figure 14. It can be seen that, for LSBG, the observed data are broadly consistent within errors with the known $M-\sigma_*$ established based on local normal galaxies and AGNs (Tremaine et al. 2002, dashed line). However, a statistically meaningful result has to await the availability of a larger sample with both black hole mass and σ_* measurements.

6. Conclusion

We have performed detailed spectral analysis of 194 LSBGs from the Impey et al. (1996) APM LSBG sample which have been observed spectroscopically by the SDSS DR5. Our work improves upon previous spectroscopic studies on LSBGs with high and homogeneous quality SDSS spectra and elaborate spectral analysis, which includes subtraction of host galaxy starlight spectra, and deblending narrow and broad components of the Balmer lines and doublets. These improvements allow us to carry out, for the first time, reliable spectral classification of nuclear activities of LSBGs based on the BPT classification schemes in a rigorous way. We also identified three secured broad line AGNs in LSBGs, and clarified a few spurious ones claimed in previous work.

We found that, the majority (68%) of the LSBGs are emission line galaxies. The most abundant class is star-forming galaxies (52%) characteristic of HII emission line spectra. Within the APM-SDSS sample, about 15% LSBGs show emission line spectra characteristic of AGNs, including Seyfert galaxies, LINERs, and galactic nuclei composed of an AGN and central star-forming region. Such a fraction of AGNs is significantly lower than that found in local normal galaxies. This result holds true even within each morphological type from Sa to Sc. Our results do not support the high AGN fractions in LSBGs suggested in some of the previous studies (Sprayberry et al. 1995; Schombert 1998), but is qualitatively consistent with that found by Impey01. We found that the

fraction of AGNs depends strongly both on the stellar velocity dispersion of the bulges and on the physical size of the galaxies, the two of which are coupled with each other. We interpret the low AGN fraction in LSBGs in terms of the postulation that, compared to HSBGs, LSBGs possess relatively lower bulge masses, or a lower fraction of galaxies with bulges, even within the same morphological type. This hypothesis can be tested in further observations in the future.

Compared to AGNs of HSBGs, AGNs in LSBGs tend to have relatively lower electron density and lower dust extinction in the NLR. As in HSBGs, the width of narrow emission lines in active nuclei of LSBGs is a good tracer of the stellar velocity dispersion in the galactic bulge. The black hole masses of the 3 broad line AGNs in LSBGs are broadly consistent within errors with the well known $M-\sigma_*$ relation found for nearby galaxies and AGNs.

7. Acknowledgements

This work is supported by the National Natural Science Foundation of China NSF-10533050 and NSF-10373004. This work has made use of the data products of the SDSS. We thank the anonymous referee for reviewing this paper. We also thank Jianguo Wang and Hongyan Zhou for their checking the SDSS spectra and valuable suggestion. We gratefully thank Poon Helen for her careful English correction.

A. SDSS starlight spectral modeling

The spectra are first corrected for Galactic extinction using the extinction map of Schlegel et al. (1998) and the reddening curve of Fitzpatrick (1999), and transformed into the rest frame using the redshift provided by the SDSS pipeline. Then host-galaxy starlight and AGN continuum, as well as the optical Fe II emission complex are modeled as

$$S(\lambda) = A_{host}(E_{B-V}^{host}, \lambda) A(\lambda) + A_{nucleus}(E_{B-V}^{nucleus}, \lambda) [bB(\lambda) + c_b C_b(\lambda) + c_n C_n(\lambda)] \quad (\text{A1})$$

where $S(\lambda)$ is the observed spectrum. $A(\lambda) = \sum_{i=1}^6 a_i IC_i(\lambda, \sigma_*)$ represents the starlight component modeled by our 6 synthesized galaxy templates, which had been built up from the spectral template library of Simple Stellar Populations (SSPs) of Bruzual & Charlot (2003, hereafter BC03) using our new method based on the Ensemble Learning Independent Component Analysis (EL-ICA) algorithm. The details of the galaxy templates and their applications are presented in (Lu et al. 2006). $A(\lambda)$ was broadened by convolving with a Gaussian of width σ_* to match the stellar velocity dispersion of the host galaxy. The un-reddened nuclear continuum is assumed to be $B(\lambda) = \lambda^{-1.7}$ as given in Francis (1996). We modeled the optical Fe II emission, both broad and narrow, using the spectral data of the Fe II multiplets for IZwI in the $\lambda\lambda 3535\text{--}7530\text{\AA}$ range provided by Veron-Cetty et al. (2004)[Table A1,A2]veron04. We assume that the broad F_e II lines (C_b in Eq.1)

have the same profile as the broad $H\beta$ line, and the narrow Fe II lines (C_n), both permitted and forbidden, have the same profile as the that of the narrow $H\beta$ component, or of $[O III]\lambda 5007$ if $H\beta$ is weak. $A_{host}(E_{B-V}^{host}, \lambda)$ and $A_{nucleus}(E_{B-V}^{nucleus}, \lambda)$ are the color excesses due to possible extinction of the host galaxy and the nuclear region, respectively, assuming the extinction curve for the Small Magellanic Cloud of Pei (1992). The fitting is performed by minimizing the χ^2 with E_{B-V}^{host} , $E_{B-V}^{nucleus}$, a_i , σ_* , b , c_b and c_n being free parameters. To account for possible error of the redshifts provided by the SDSS pipeline, in practice we loop possible redshifts near the SDSS redshift, spaced every 5 km s^{-1} . We fit and subtracted the above model from the SDSS spectra.

REFERENCES

- Baldwin, A. J., Phillips, M. M., & Terlevich, R. 1981, *PASP*, 93, 5
- Becker, R. H., White, R. L., & Helfand, D. J. 1995, *ApJ*, 450, 559
- Beijersbergen, M., de Blok, W. J. G., van der Hulst, J. M. 1999, *A&A*, 351, 903
- Bell, E. F., Barnaby, David., Bower, Richard G., et al. 2000, *MNRAS*, 312, 470
- Bruzual, G., & Charlot, S. 2003, *MNRAS*, 344, 1000 (BC03)
- Dalcanton, J. J., Spergel, D. N., & Summers, F. J. 1997, *ApJ*, 482, 659
- de Vaucouleurs, Gerard., de Vaucouleurs, Antoinette., Corwin, Herold G., Jr., Buta, Ronald J., Paturel, Georges., & Fouque, Pascal. 1991, *trcb.book*
- de Blok, W. J. G.; McGaugh, S. S.; van der Hulst, J. M. 1996, *MNRAS*, 283, 18
- de Blok, W. J. G., & McGaugh, S. S. 1996, *ApJ*, 469, L89
- Dong, X.-B., Zhou, H.-Y., Wang, T.-G., Wang, J.-X., Li, C., & Zhou, Y.-Y. 2005, *ApJ*, 620, 629
- Ferrarese, Laura., & Merritt, David. 2000, *ApJ*, 539L, 9
- Filippenko, A. V., & Sargent, W. L. W. 1988, *ApJ*, 324,134
- Fitzpatrick, E. L. 1999, *PASP*, 111, 63
- Francis, P.J. 1996, *Publications of the Astronomical Society of Australia*, 13, 212
- Freeman, K. 1970, *ApJ*, 169, 811
- Galaz, Gaspar., Villalobos, Alvaro., Infante, Leopoldo., Donzelli, Carlos. 2006, *AJ*, 131, 2035
- Gebhardt, Karl., et al. 2000, *ApJ*, 539L, 13
- Green, J. E., Ho, L. C. 2007, *ApJ*, 670, 92

- Green, J. E., Ho, L. C. 2007, ApJ, 667, 131
- Hao et al. 2005, AJ, 129, 1783
- Heckman T. M., 1980, A&A, 87, 152
- Hinz, J. L., Rieke, M. J., Rieke, G. H., Willmer, C. N. A., Misselt, K., Engelbracht, C. W., Blaylock, M., Pickering, T. E. 2007, ApJ, 663, 895
- Ho, L. C., et al. 1997, ApJ, 487, 568
- Ho, L. C., et al. 1997, ApJs, 112, 315
- Impey, C., & Bothun, G. 1989, ApJ, 341, 89
- Impey, C., et al. 1996, ApJS, 105, 209
- Impey, C., Bothun, G. 1997, ARA&A, 35, 267
- Impey, C., Burkholder, V., & Sprayberry, D. 2001, AJ, 122, 2341
- Kaspi, Shai., Smith, Paul S., Netzer, Hagai, Maoz, Dan, Jannuzi, Buell T., Giveon, Uriel. 2000, ApJ, 533, 631
- Kauffmann, G., Heckman, T., Tremonti, C., Brinchmann, J. 2003, MNRAS, 346, 1055
- Kennicutt, Robert C., Jr. 1989, ApJ, 344, 685
- Kewley, L. J., Dopita, M. A., Sutherland, R. S., Heisler, C. A., & Trevena, J. 2001, ApJ, 556, 121
- Kewley, L. J., Groves, B., Kauffmann, G., & Heckman, T. 2006, MNRAS, 372, 961
- Lu, H., Zhou, H., Wang, J., Wang, T., Dong, X., Zhuang, Z., & Li, C. 2006, AJ, 131, 790
- McGaugh, S., Bothun, G., & Schombert, J. 1995, AJ, 110, 573
- Monnier Ragaigne, D., et al. 2003, A&A, 405, 99
- Morshidi-Esslinger, Z., et al. 1999, MNRAS, 304, 297
- O’Neil, K., Bothun, G. D., & Schombert, J. 1998, AJ, 116, 2776
- Osterbrock, Donald. E. & Ferland, Gary. J., 2006, Astrophysics of Gaseous Nebulae and Active Galactic Nuclei, Second Edition.
- Pei, Y. C. 1992, ApJ, 395,130
- Schaye, Joop. 2004, ApJ, 609, 667
- Schlegel, D. J., Finkbeiner, D. P., & Davis, M. 1998, ApJ, 500, 525

- Schombert, James M., Bothun, Gregory D., Impey, Chris D., & Mundy, Lee G. 1990, *AJ*, 100, 1523
- Schombert, J. 1998, *AJ*, 116, 1650
- Sprayberry, D., et al. 1995, *AJ*, 109, 558
- Stoughton, Chris., et al. 2002, *AJ*, 123, 485
- Strauss, M., et al. 2002, *AJ*, 124, 1810
- Tremaine, S., et al. 2002, *ApJ*, 574, 740
- van der Hulst, J., et al. 1993, *AJ*, 106, 548
- Veilleux, S., & Osterbrock, D. E. 1987, *ApJS*, 63, 295
- Veron-Cetty, M.-P., Joly, M., & Veron, P. 2004, *A&A*, 417, 515
- Vestergaard, M., & Peterson, B. M. 2006, *ApJ*, 641, 689
- Xu, D. W., et al. 2007, *ApJ*, 670, 60
- Yuan, W., et al. 2004, *MNRAS*, 353, L29
- Zhou, H., Wang, T., Yuan, W., Lu, H., Dong, X., Wang, J., & Lu, Y. 2006, *ApJS*, 166, 128

Table 1. Spectral parameters and classification of the 131 emission-line LSBGs

Name	Z	[OII] ^a λ3727	Hβ ^a narrow	[O III] ^a λ5007	[OI] ^a λ6300	Hα ^a narrow	[NII] ^a λ6583	[SII] ^a λ6717/λ6731	FWHM[NII] ^b km s ⁻¹	σ _* ^c km s ⁻¹	Type ^d
001455.1+001508.3	0.039	289.6	400.6	122.2	61.1	1859.1	1062.5	282.2/261.8	226.7	111.9	composite
001558.2-001812.6	0.039	***	43.6	89.1	46.0	163.3	129.0	88.0/ 68.1	299.5	170.3	LINER
001930.7-003606.3	0.033	***	223.6	312.3	16.7	623.7	130.6	133.1 /93.2	172.2	***	hii
002149.8-001929.4	0.044	***	4.1	6.0	***	12.4	3.5	4.7/3.1	163.6	***	hii
002534.4+005048.6	0.018	***	36.3	15.9	7.0	114.0	37.9	30.9/21.9	161.2	***	hii
003143.3+005402.8	0.018	75.9	12.7	13.4	***	43.9	12.4	13.2/12.7	169.6	***	hii
005042.7+002558.3	0.068	71.8	30.1	98.2	20.0	147.8	130.6	41.8/ 38.2	424.0	163.4	S2
005257.2+002317.4	0.035	***	48.4	20.4	6.8	172.4	54.8	44.1/28.2	166.7	***	hii
005257.8+002207.6	0.034	***	1080.2	3204.9	81.7	4067.3	609.2	424.7/274.9	179.4	147.7	hii
005342.7-010506.6	0.047	***	132.5	1179.5	143.7	349.7	594.8	8.1 /8.1	318.9	140.4	LINER
005509.0-010247.3	0.046	41.8	32.8	46.5	***	65.1	77.5	29.3/21.2	367.5	170.6	LINER
005848.9+003514.0	0.018	***	163.2	53.3	15.2	670.5	287.9	107.1/ 93.1	196.0	***	hii
005855.5+010017.4	0.018	182.5	713.7	3600.7	31.9	2469.7	65.8	159.3/114.4	155.1	438.1	hii
010550.2+001432.2	0.048	***	151.6	40.8	18.3	617.6	203.4	93.8/ 71.2	184.8	76.2	hii
011050.8+001153.3	0.018	***	93.9	19.4	5.0	409.4	149.5	63.9/ 45.1	165.0	***	hii
011244.8+003935.1	0.065	35.9	38.1	15.1	7.6	139.2	53.8	30.9/ 24.2	175.1	96.0	hii
011310.0+005012.1	0.033	64.9	11.4	6.4	***	42.1	11.1	13.4/10.3	160.8	***	hii
011448.7-002946.1	0.034	***	346.6	748.1	46.8	1478.3	704.8	203.8/135.5	259.7	149.7	S1
012121.3+000525.5	0.013	***	31.4	24.5	13.7	65.6	17.0	27.7/14.9	184.5	84.1	hii
012539.7+011041.2	0.020	***	53.3	12.1	11.9	207.1	81.6	39.3/ 30.5	166.4	***	hii
021532.0-001727.4	0.026	63.0	16.6	9.4	***	46.9	11.5	12.4/8.5	169.5	***	hii
022606.7-001954.9	0.021	38.6	22.5	39.7	***	91.9	89.3	36.9/26.8	281.4	112.1	LINER
022933.9+002223.3	0.021	***	14.0	25.8	***	31.9	6.6	11.7/8.7	189.1	***	hii
023143.4+001736.5	0.021	***	18.5	8.4	7.4	54.8	16.3	17.2/13.1	171.1	***	hii
023238.1+003539.3	0.022	59.2	1018.5	3510.1	68.7	2862.3	215.1	325.9/218.8	170.5	98.1	hii
023239.3+003702.4	0.021	29.3	172.7	86.8	29.8	669.1	269.2	121.1 /75.1	189.0	***	hii
023601.0+002512.8	0.009	***	14.8	9.8	***	36.3	13.4	15.0/9.8	162.4	***	hii
024056.6+001445.6	0.027	***	11.3	10.1	10.2	29.0	9.1	9.8/5.4	179.3	***	hii
024227.3+010214.4	0.046	***	35.4	17.2	5.8	152.9	70.2	30.3/24.2	244.4	100.0	hii
024547.6-001427.1	0.023	***	8.4	7.5	***	18.4	9.2	9.0/5.7	166.6	***	composite
024631.1-002158.5	0.051	***	12.8	4.9	***	54.5	20.4	12.6/7.4	159.3	***	hii
031859.4+011347.5	0.038	198.3	6.5	9.4	***	27.4	5.4	9.0/5.4	142.3	***	hii
032910.8-010246.3	0.036	***	7.9	4.7	***	19.3	3.8	5.2/3.5	152.3	***	hii
033507.2-005237.9	0.038	***	5.9	18.0	***	25.8	9.5	8.3/3.1	166.6	***	composite

Table 1—Continued

Name	Z	[OII] ^a λ3727	Hβ ^a narrow	[O III] ^a λ5007	[OI] ^a λ6300	Hα ^a narrow	[NII] ^a λ6583	[SII] ^a λ6717/λ6731	FWHM[NII] ^b km s ⁻¹	σ _* ^c km s ⁻¹	Type ^d
034907.9+010943.4	0.014	70.8	923.3	2489.0	40.7	2931.6	280.3	315.4/224.2	163.5	***	hii
035326.2+005030.5	0.038	100.4	33.4	32.2	***	122.4	73.1	25.2/ 19.9	192.0	113.1	composite
091613.8+004202.3	0.038	43.7	320.2	227.7	44.4	1386.2	668.9	225.7/183.5	285.1	121.7	composite
091745.3+010319.5	0.027	36.8	37.1	22.2	7.9	140.3	39.3	34.4/ 22.2	165.8	97.5	hii
091955.2-003528.9	0.029	***	10.2	15.9	***	49.7	8.1	15.3/10.8	162.7	***	hii
092346.4+024510.7	0.017	***	57.3	89.6	8.9	194.4	25.7	34.9/26.7	173.4	***	hii
093223.1+023251.4	0.017	617.8	15.5	30.7	***	52.4	6.0	10.8/7.9	167.1	***	hii
095959.3+003817.6	0.033	33.9	67.1	100.3	13.6	260.2	43.3	61.2/ 43.3	170.4	***	hii
100440.8+002211.6	0.045	106.5	19.8	28.7	***	52.2	67.2	43.1/ 22.3	339.1	124.8	LINER
101105.2+011326.7	0.033	***	63.5	19.1	***	320.3	105.7	39.8/ 32.1	224.5	98.0	hii
101117.9+002632.6	0.012	42.4	201.9	34.5	15.0	841.1	281.6	93.5/ 71.6	173.5	***	hii
101853.9+021439.2	0.046	817.8	36.2	30.2	***	127.3	30.7	32.6/ 19.3	161.4	***	hii
102533.3+021903.6	0.064	459.7	50.2	29.4	***	186.4	82.1	26.8/ 19.0	267.2	99.3	hii
103135.1-005624.5	0.033	***	15.6	12.6	***	43.4	16.7	15.1/10.7	191.0	***	hii
103226.9+023318.0	0.022	21.0	20.6	25.4	5.9	82.9	19.4	27.7/17.8	171.4	***	hii
103321.0+023658.1	0.029	316.9	329.1	64.6	39.6	1675.2	594.3	229.8/182.1	213.8	71.7	hii
103723.6+021845.5	0.040	34.7	112.0	250.2	127.6	411.7	400.0	256.4/205.3	390.0	209.8	LINER
103725.7+020443.1	0.074	26.5	20.5	16.9	6.5	104.5	52.9	31.2/ 22.5	358.9	155.7	composite
103727.7+020521.9	0.073	***	9.0	39.2	42.9	73.9	111.4	57.4/39.7	485.0	196.0	LINER
103825.5-000104.2	0.019	***	14.3	12.0	3.2	50.2	10.6	19.4/12.2	170.7	***	hii
104405.9-005744.5	0.027	40.6	7.4	8.6	***	25.5	4.3	7.4/5.2	166.4	***	hii
104501.2+013855.3	0.028	9.0	13.1	10.9	***	36.6	8.6	10.6/8.6	175.5	***	hii
104509.1+000433.4	0.094	***	12.1	18.5	15.1	19.9	23.3	16.8/10.1	345.2	180.6	LINER
104614.9+000300.9	0.047	280.2	494.9	355.0	63.1	1817.9	539.2	357.4/271.5	192.2	101.6	hii
104634.3+014627.8	0.022	***	10.4	8.1	***	26.0	3.8	6.4/6.1	162.3	***	hii
104819.9-000119.1	0.039	24.4	10.3	4.2	3.3	52.3	22.7	12.4/8.2	172.9	61.9	hii
105318.6+023733.7	0.003	85.3	185.5	371.0	13.5	556.8	17.7	56.4/ 36.2	154.2	***	hii
110700.5+001022.3	0.038	***	13.1	17.2	***	33.8	6.4	7.4/5.6	176.5	***	hii
111549.4+005137.5	0.046	36.0	161.2	219.8	290.0	972.7	815.5	641.4/473.4	554.6	187.7	LINER
111849.6+003709.5	0.025	109.6	123.3	33.8	15.7	462.7	162.3	81.6 /56.1	188.0	***	hii
112409.2+004202.0	0.026	739.0	58.6	18.4	5.7	246.4	89.2	40.5/ 27.6	177.3	***	hii
112712.2-005940.8	0.003	390.8	74.3	109.1	9.3	200.4	16.4	46.8/ 35.4	158.4	***	hii
112718.8-010335.5	0.041	255.7	7.3	5.4	***	21.0	5.9	6.8/4.3	159.5	***	hii
113245.4-004427.8	0.022	***	34.5	24.7	4.6	134.1	29.5	39.1/27.0	155.7	***	hii

Table 1—Continued

Name	Z	[OII] ^a λ3727	Hβ ^a narrow	[O III] ^a λ5007	[OI] ^a λ6300	Hα ^a narrow	[NII] ^a λ6583	[SII] ^a λ6717/λ6731	FWHM[NII] ^b km s ⁻¹	σ _* ^c km s ⁻¹	Type ^d
113505.0+023304.1	0.017	28.5	207.4	424.9	17.0	706.4	97.2	107.4 /78.7	157.0	83.8	hii
115336.9+020957.8	0.040	***	9.6	21.2	***	39.0	4.4	10.4/5.0	164.0	***	hii
115342.8-013935.6	0.011	71.3	33.3	56.2	***	93.0	15.0	24.2/13.9	166.5	***	hii
115412.1-002856.7	0.006	132.0	9.8	24.3	***	33.1	2.6	4.5/3.0	159.6	***	hii
115801.1-021038.3	0.082	90.4	13.4	20.0	***	22.3	30.9	9.6/22.7	409.8	187.3	LINER
115924.6+012602.6	0.047	***	25.8	5.3	***	73.6	29.0	12.2/11.4	207.0	64.3	hii
120804.0+004151.3	0.020	38.7	103.6	100.1	9.5	301.9	66.0	57.6/ 38.3	160.0	***	hii
120806.2-023156.0	0.026	***	14.2	13.9	***	39.0	14.5	12.7/9.3	153.3	***	hii
121159.5+012100.1	0.021	***	82.5	56.3	11.1	273.7	67.6	70.9/ 49.5	168.6	67.0	hii
121203.3-003621.7	0.035	22.9	708.0	1899.6	46.7	2308.2	223.9	266.7/188.8	192.0	336.1	hii
121248.3-024328.6	0.038	***	247.9	169.9	89.6	1228.5	670.2	331.6/293.6	379.4	169.8	composite
121431.0+021000.7	0.074	***	18.9	7.4	***	73.9	26.2	9.3/8.6	189.5	***	hii
121604.5+011049.6	0.050	***	237.1	74.6	47.7	1175.7	488.3	186.1 /148.1	260.9	98.7	hii
121638.7-012706.7	0.003	1975.4	29.4	45.7	6.0	84.4	4.7	8.9/6.3	177.9	***	hii
122033.8+004717.6	0.007	***	81.3	96.8	11.4	249.9	38.7	52.4/ 38.7	160.2	***	hii
122404.9+011123.3	0.024	1001.8	413.2	75.1	24.8	1839.0	636.5	228.4/185.3	227.7	107.4	hii
122610.0-010923.1	0.042	***	44.3	25.6	***	151.2	68.8	36.9/26.0	174.2	***	composite
122801.7+013629.5	0.077	***	57.6	18.3	9.6	252.2	86.8	39.1/30.2	175.6	***	hii
122912.9+004903.7	0.079	***	30.7	200.7	11.5	97.1	91.3	33.1/ 24.5	298.8	168.2	S1
122921.6+010325.0	0.023	23.2	166.0	32.9	17.3	683.7	212.1	121.6 /90.9	171.9	67.4	hii
125323.8-002523.5	0.048	***	14.7	6.3	11.8	100.7	40.9	23.9/13.6	172.4	***	hii
130058.7-000139.1	0.004	***	1330.1	479.9	75.3	5002.2	1602.0	821.0/615.2	181.1	74.9	hii
130243.5+003949.9	0.041	***	90.6	22.9	13.2	417.6	202.1	62.4/ 48.9	205.5	95.2	hii
130316.0+012807.1	0.041	49.4	39.3	13.2	***	202.0	79.5	38.7/ 30.8	197.0	93.8	hii
130338.9+024335.2	0.071	***	22.9	51.5	***	57.4	44.0	36.6/21.9	405.9	207.5	S2
131004.7+005655.7	0.019	***	8.2	4.9	***	20.1	4.4	5.9/4.0	198.4	***	hii
131809.3+001322.1	0.032	***	34.8	30.9	***	120.8	36.2	37.5/24.5	164.0	***	hii
132340.7+012142.5	0.057	***	46.8	57.7	29.8	296.5	204.4	76.0/ 58.4	271.3	132.6	composite
132955.8+013238.6	0.004	***	79.7	136.7	9.7	251.5	19.0	47.2/ 32.0	163.1	***	hii
133032.0-003613.5	0.054	***	290.5	856.5	96.8	1553.5	995.0	334.8/270.8	299.5	158.5	S2
133305.3-010208.9	0.012	34.5	181.7	287.2	***	835.4	1194.3	616.3/473.9	378.0	133.3	LINER
135658.2-010606.1	0.031	***	30.0	24.5	***	93.5	21.5	16.5/11.1	173.9	***	hii
140043.0-003020.5	0.012	48.8	104.2	164.3	8.9	285.2	43.7	49.8/ 37.0	157.2	***	hii
140126.7-024245.9	0.030	63.0	26.2	14.1	***	113.3	29.1	27.9/ 17.8	157.2	70.7	hii

Table 1—Continued

Name	Z	[OII] ^a λ3727	Hβ ^a narrow	[O III] ^a λ5007	[OI] ^a λ6300	Hα ^a narrow	[NII] ^a λ6583	[SII] ^a λ6717/λ6731	FWHM[NII] ^b km s ⁻¹	σ _* ^c km s ⁻¹	Type ^d
140127.5+015822.6	0.024	***	21.6	30.9	6.6	82.1	14.9	22.7/19.0	172.5	***	hii
140320.7-003259.8	0.025	56.3	489.0	78.8	43.1	2173.5	857.7	300.1/226.6	198.5	78.7	hii
140321.1-003256.9	0.025	2265.5	384.0	95.1	23.9	1498.4	485.7	216.1/148.2	168.0	66.2	hii
140831.6-000737.4	0.025	95.6	39.9	17.2	9.8	136.9	50.8	39.3/ 24.0	171.3	***	hii
141130.1+004159.9	0.053	665.4	9.4	12.7	***	39.3	8.3	12.7/6.0	177.5	***	hii
141132.9-031311.1	0.030	***	87.0	22.6	***	386.5	133.4	52.4/ 38.3	226.2	99.6	hii
141140.7-010307.8	0.024	14.7	6.9	12.7	***	36.0	4.7	9.9/6.2	152.9	***	hii
143127.2-024009.0	0.024	33.0	25.6	12.6	***	43.5	6.1	10.8/9.0	177.6	***	hii
143421.4+013626.5	0.031	***	26.2	16.8	2.5	70.1	15.8	19.9/10.1	167.8	***	hii
143638.6+000702.6	0.030	13.0	14.3	6.6	***	42.1	15.1	13.6/10.8	177.4	***	hii
143846.3+010657.7	0.083	***	20.5	62.8	15.5	151.2	118.6	70.1/ 52.7	547.8	271.0	S2
144245.9-002103.9	0.006	54.9	221.9	496.9	27.6	661.0	80.4	132.3 /89.8	170.4	***	hii
144500.2+012430.8	0.034	***	22.1	14.1	***	95.9	55.9	20.3/17.0	212.4	88.8	composite
144525.4+001404.3	0.038	***	21.6	16.2	6.6	87.6	32.7	12.6/9.0	178.7	70.4	hii
144620.6-010520.0	0.029	***	786.3	3185.1	59.9	2697.6	110.3	269.5/188.7	158.6	***	hii
144702.4-022307.2	0.030	***	8.8	5.1	***	22.6	6.3	6.1/6.3	164.0	***	hii
144856.4-004338.0	0.028	***	25.3	30.2	***	87.1	15.0	19.3/15.8	168.2	***	hii
144902.6+022611.2	0.034	***	11.2	8.2	***	34.8	21.0	10.7/4.2	182.0	***	composite
144923.4-013333.4	0.027	***	19.9	23.3	***	58.5	8.7	14.8/8.6	163.7	***	hii
145325.3+021810.9	0.027	***	5.7	10.3	***	20.3	2.9	7.4/4.7	146.4	***	hii
145423.9-010747.3	0.023	***	19.4	22.6	***	54.6	10.1	14.9/10.5	172.6	***	hii
231221.0-010542.4	0.026	***	13.3	14.5	***	39.3	10.3	13.9/9.3	165.5	***	hii
231501.6+000420.1	0.051	***	23.8	39.0	33.1	77.2	88.8	45.6/42.6	338.2	121.6	LINER
231815.7+001540.2	0.030	***	186.0	514.3	52.6	756.1	483.6	220.1 /178.5	274.9	124.5	S1
231952.0+011305.0	0.030	***	54.4	55.7	8.6	160.1	28.4	44.2/27.3	169.6	***	hii
232021.2-001819.3	0.025	***	14.5	15.4	***	49.2	12.7	17.7/8.3	162.7	***	hii
232151.8-004126.8	0.024	***	53.9	15.1	6.6	244.9	77.7	47.4/35.3	173.1	81.2	hii
233646.8+003724.5	0.009	27.3	125.8	315.5	5.4	356.2	37.4	49.4/ 34.1	155.0	***	hii
234422.2+000547.0	0.022	***	17.8	4.6	***	21.9	8.4	10.9/5.2	172.9	***	hii

^aIn units of 10⁻¹⁷ erg cm⁻² s⁻¹

^bThe full width at half maximum (FWHM), in units of km s⁻¹

^cThe measured stellar velocity dispersion of galactic bulge, in units of km s⁻¹

^dThe classification of emission-line nuclear based on the narrow line fluxes ratios.

Table 2. Parameters of broad Balmer lines of 3 LSB AGNs with broad emission lines.

Name SDSS	$f[\text{H}\beta]^e$ $\lambda 4861^{broad}$	FWHM ($\text{H}\beta$) km s^{-1}	$f[\text{H}\alpha]^e$ $\lambda 6563^{broad}$	FWHM ($\text{H}\alpha$) km s^{-1}	σ_* km s^{-1}	M_{BH}^f M_\odot
J011448.7-002946.1	743.4	3195	2769.4	2418	84.7	2.8×10^6
J122912.9+004903.7	298.9	7400	1192.6	4750	138.2	2.0×10^7
J231815.7+001540.2	***	***	1037.4	3756	98.5	3.4×10^6

^eIn units of $10^{-17} \text{ erg cm}^{-2} \text{ s}^{-1}$

^fEstimated black hole masses based on equations from Greene & Ho (2007)

Table 3. Properties of the LSBGs with an AGN.

Name	Name	μ_0^B ²	μ_e ³	B_{total} ⁴	$\log(M_{HI})$ ⁵	R_e ⁶	M_B ⁷	Hubble Type ⁸
0012–0001	J001455.1+001508.3	20.8	21.5	15.5		5.7	–19.9	Sb
0013–0034	J001558.2–001812.6	20.3	23.3	14.5	10.18	18.4	–20.9	Sc
0048+0009	J005042.7+002558.3	21.3	22.3	15.8		6.2		Sb
0051–0121	J005342.7–010506.6	21.6	22.9	15.9		7.2		SBc
0052–0119	J005509.0–010247.3	19.9	23.4	14.9		11.9	–20.8	Sd
0112–0045	J011448.7–002946.1	21.5	22.0	14.9		8.9		Interacting
0223–0033	J022606.7–001954.9	22.1	23.3	14.5	9.83	18.3	–19.5	Sc
0243–0027	J024547.6–001427.1	22.6	24.2	17.0		8.4		Sc
0332–0102	J033507.2–005237.9	22.9	23.9	17.3		6.7		Sc
0350+0041	J035326.2+005030.5	21.9	23.5	16.1	9.60	9.7	–19.2	Sc
0913+0054	J091613.8+004202.3	20.4	22.6	15.5	9.68	8.2	–19.8	Sm
1002+0036	J100440.8+002211.6	20.4	23.0	15.8		6.5	–19.8	SBb
1034+0234	J103723.6+021845.5	20.2	22.0	15.4		6.5	–20.0	Interacting
1034+0220xc	J103725.7+020443.1	21.6	22.7	17.8		3.1	–19.0	Sbc
1034+0220	J103727.7+020521.9	21.0	23.8	16.1		8.8	–20.6	Sc
1042+0020	J104509.1+000433.4	21.4	23.4	16.2		9.6	–21.2	Irr
1113+0107	J111549.4+005137.5	21.4	24.5	16.2		11.4	–19.6	Interacting
1155–0153	J115801.1–021038.3	20.7	23.6	15.9		9.9	–21.1	Sc
1210–0226	J121248.3–024328.6	20.6	22.5	15.5		6.9	–19.8	Interacting
1223–0052	J122610.0–010923.1	22.5	22.8	17.3		4.4		Sa
1226+0105	J122912.9+004903.7	20.9	23.9	15.7	10.26	12.9	–21.3	Sc
1301+0259	J130338.9+024335.2	21.9	25.4	16.9		9.7	–19.7	Sc
1321+0137	J132340.7+012142.5	21.5	22.3	15.9	9.64	6.7	–20.3	Sm
1327–0020	J133032.0–003613.5	20.0	20.7	14.9		5.2	–21.2	Interacting
1330–0046	J133305.3–010208.9	18.2	19.0	11.7		8.9	–21.1	SBb
1436+0119	J143846.3+010657.7	21.2	23.1	16.2		7.5	–20.8	Sc
1442+0137	J144500.2+012430.8	22.0	22.9	16.5		6.3	–18.5	Sc
1446+0238	J144902.6+022611.2	21.8	23.4	16.0	9.73	9.5	–19.1	Sc
2312–0011	J231501.6+000420.1	20.7	21.5	15.6	9.98	5.5	–20.4	Sb
2315–0000	J231815.7+001540.2	20.8	23.0	15.0	9.71	12.3	–19.8	Sc

²Central surface brightness in B band (mag arcsec^{–2})

³Surface brightness in B band at the effective radius (mag arcsec^{–2})

⁴Total apparent magnitude in Johnson B band (mag)

⁵ogarithm of the neutral hydrogen mass in solar masses (M_\odot)

⁶Effective radius in arcseconds, defined as the radius of a circular aperture that encloses one–half the total intensity received from the galaxy (arcsec)

⁷Absolute magnitude in B band (mag)

⁸Morphological classification in the system of de Vaucouleurs et al. (1991).

Table 4. Statistics and the fraction of each type of active nuclear for the LSBG samples.

Sample	Seyfert	LINER	Transition	AGN	Star-forming	Emission-line LSBGs
LSBGs (all)	7 (4%)	12 (6%)	11 (6%)	30 (16%)	101 (52%)	131 (68%)
LSBGs ($\mu_0^B \geq 22.0$)	0 (0.3%)	1 (0.8%)	4 (3%)	5 (4%)	58 (5%)	63 (54%)
LSBGs ($\mu_0^B < 22.0$)	7 (9%)	11 (14%)	7 (9%)	25 (32%)	43 (54%)	68 (86%)

Table 5. Statistics and the fraction of AGNs in 3 morphological types of the LSBG sample ($z < 0.04$) and the HSBG comparing sample.

Sample	Sa	Sb	Sc
LSBGs	1 (14%)	6 (16%)	14 (19%)
HSBGs	25 (51%)	21 (54%)	6 (33%)

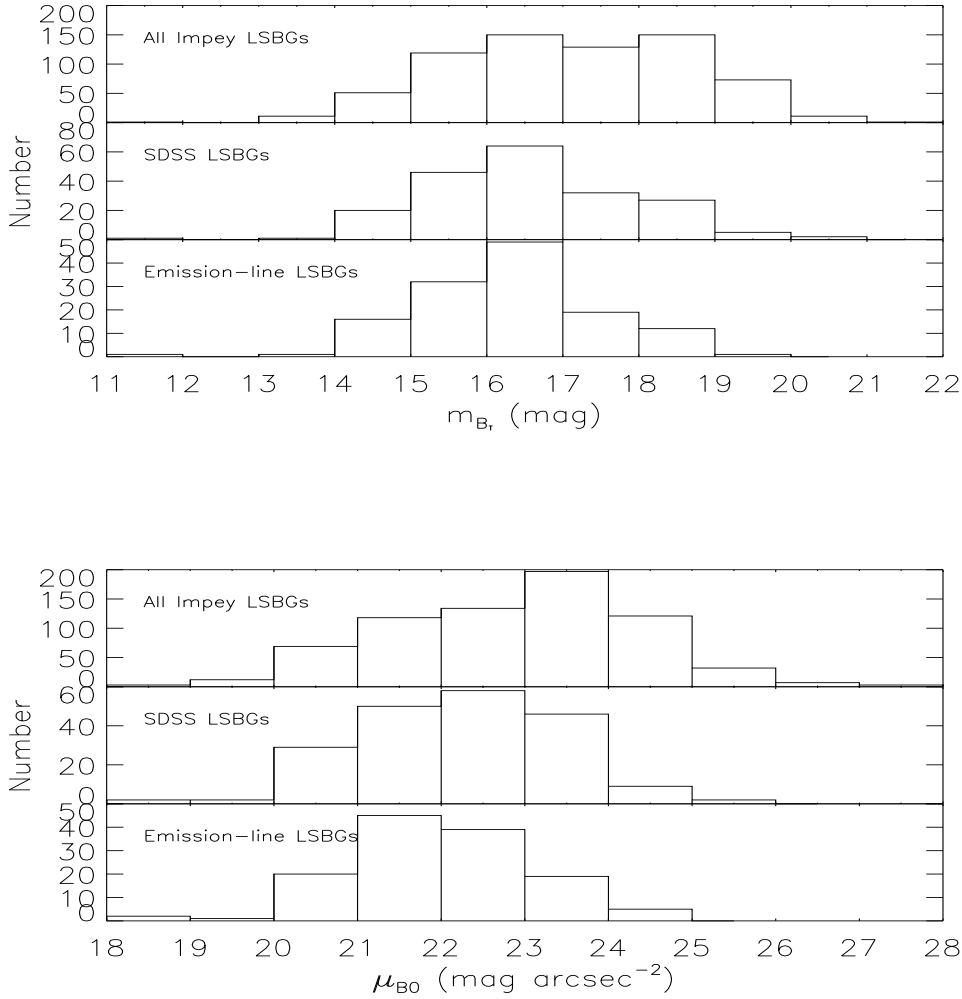


Fig. 1.— Distributions of apparent magnitude m_{B_T} in the B band, central surface brightness μ_0^B (top panel: the 693 LSBGs from the catalog of Impey et al. (1996); middle panel: the 194 APM-SDSS LSBGs; bottom panel: the 131 emission-line LSBGs with the $H\beta$, $[OIII] \lambda 5007$, $H\alpha$ and $[NII] \lambda 6583$ four lines detected with $S/N > 3$).

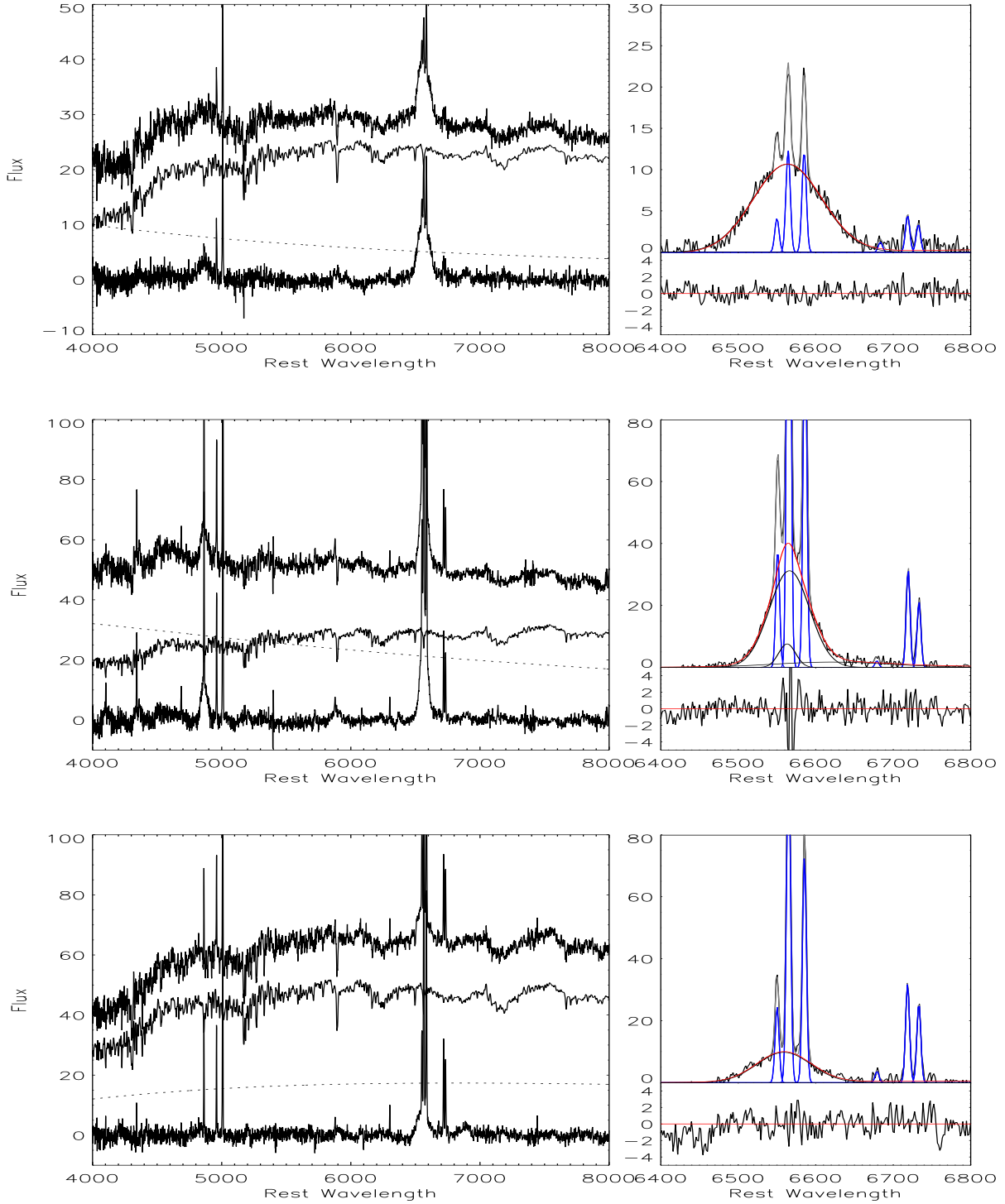


Fig. 2.— SDSS spectra of 3 LSB AGNs showing broad lines. The vertical axis is flux in unit of 10^{-17} $\text{erg s}^{-1} \text{cm}^{-2} \text{\AA}^{-1}$ and the horizontal is wavelength in \AA . The left panel shows the procedure of starlight/continuum subtraction: from top to bottom, the original spectrum, the stellar component, the nuclear continuum, and the starlight/continuum subtracted residual. The right panel shows the result of spectral fit in the $\text{H}\alpha$ -[SII] region (Top panel: original data and individual components of the fit. Blue curve: narrow component; red curve: Broad component; gray curve: final fit result. Lower panel: the residuals). Top: SDSS J122912.9+004903.7; middle: SDSS J011448.7–002946.1;

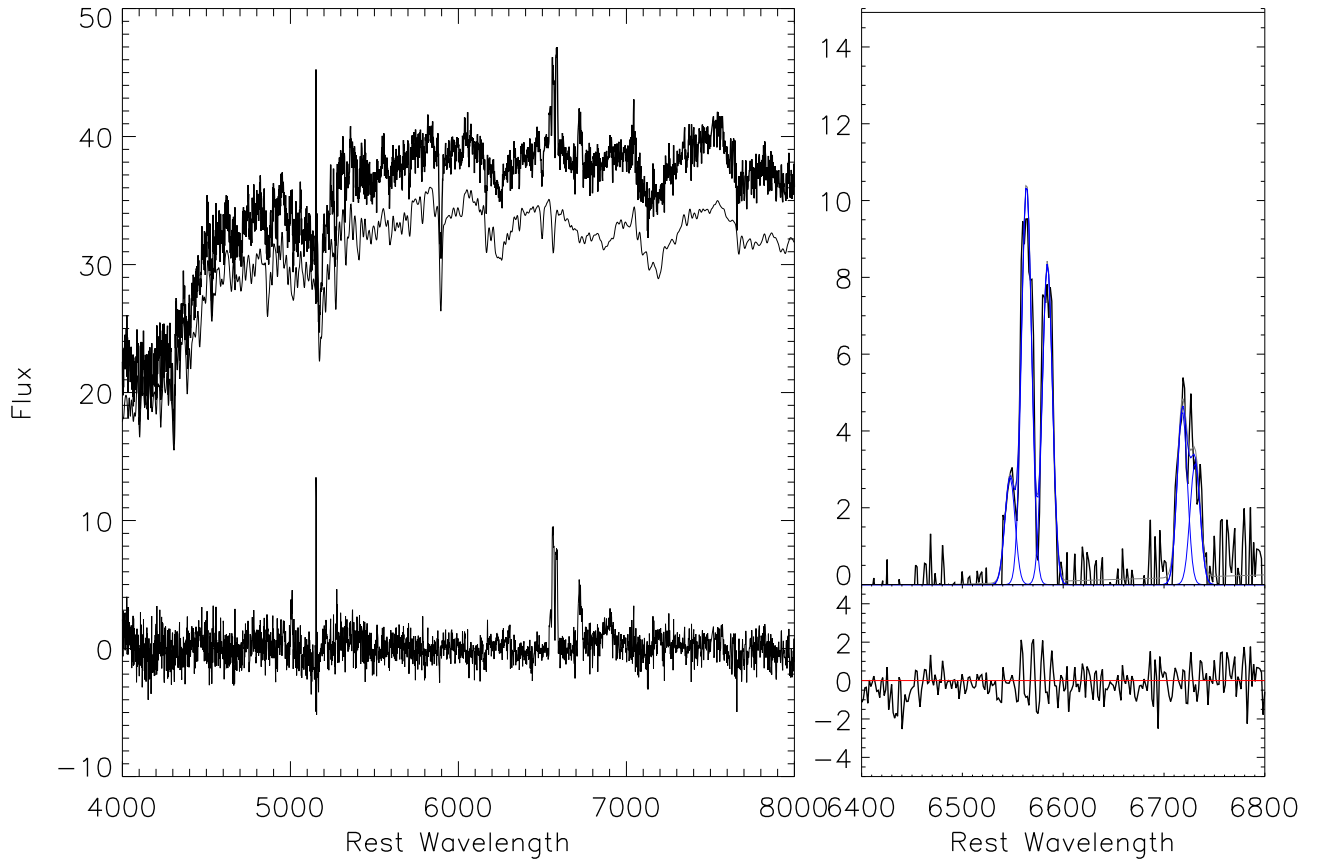


Fig. 3.— The same as Figure.2. SDSS spectrum of the LSBG 1436+0119 (SDSS J143846.3+010657.7) which was claimed to have a broad $H\alpha$ line by Impey01. No broad $H\alpha$ line is shown in the SDSS spectrum.

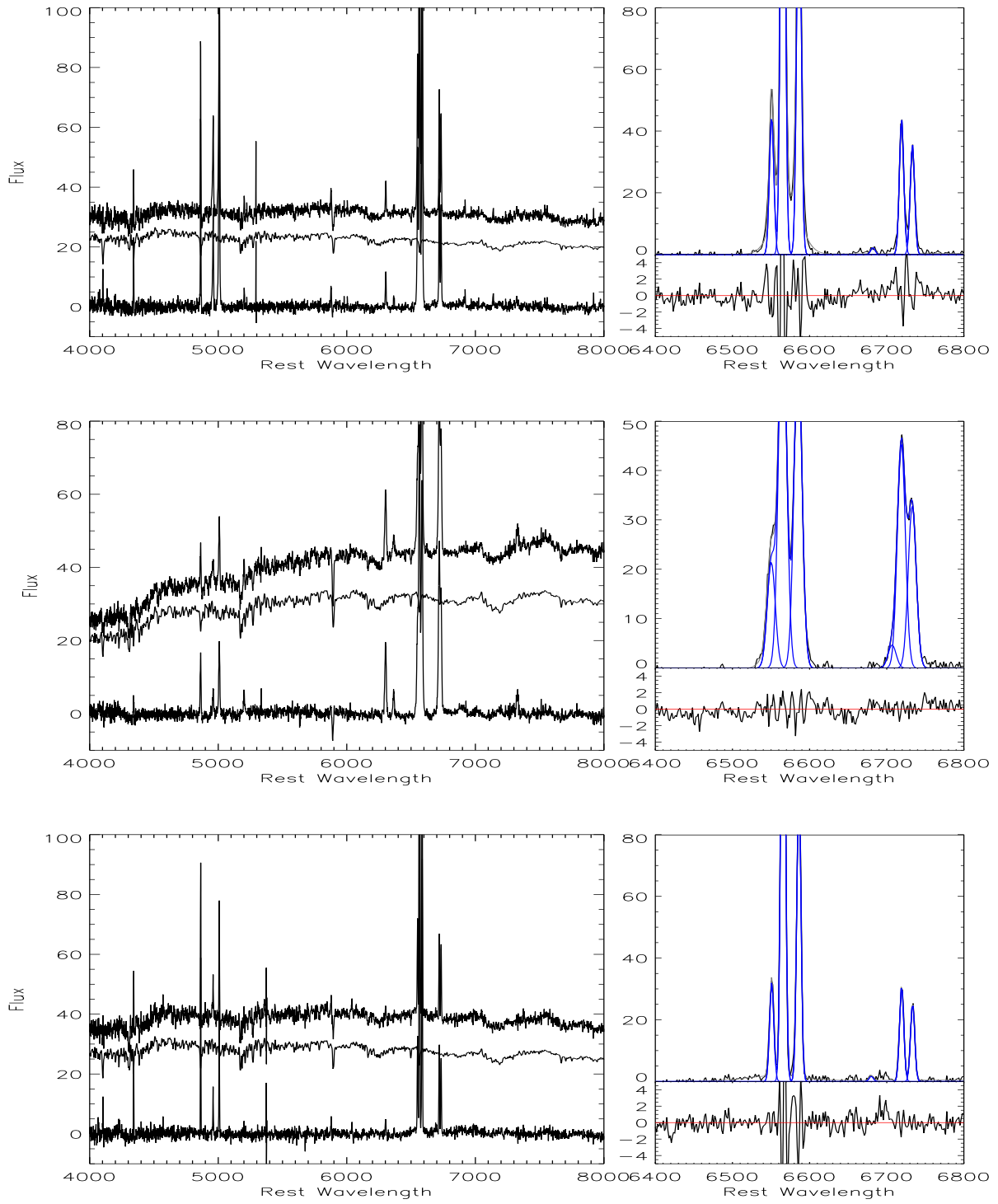


Fig. 4.— The same as Figure.2. Demonstration spectra for the 3 types of nuclear activities. Top: Seyfert 2; middle: LINER; bottom: composite.

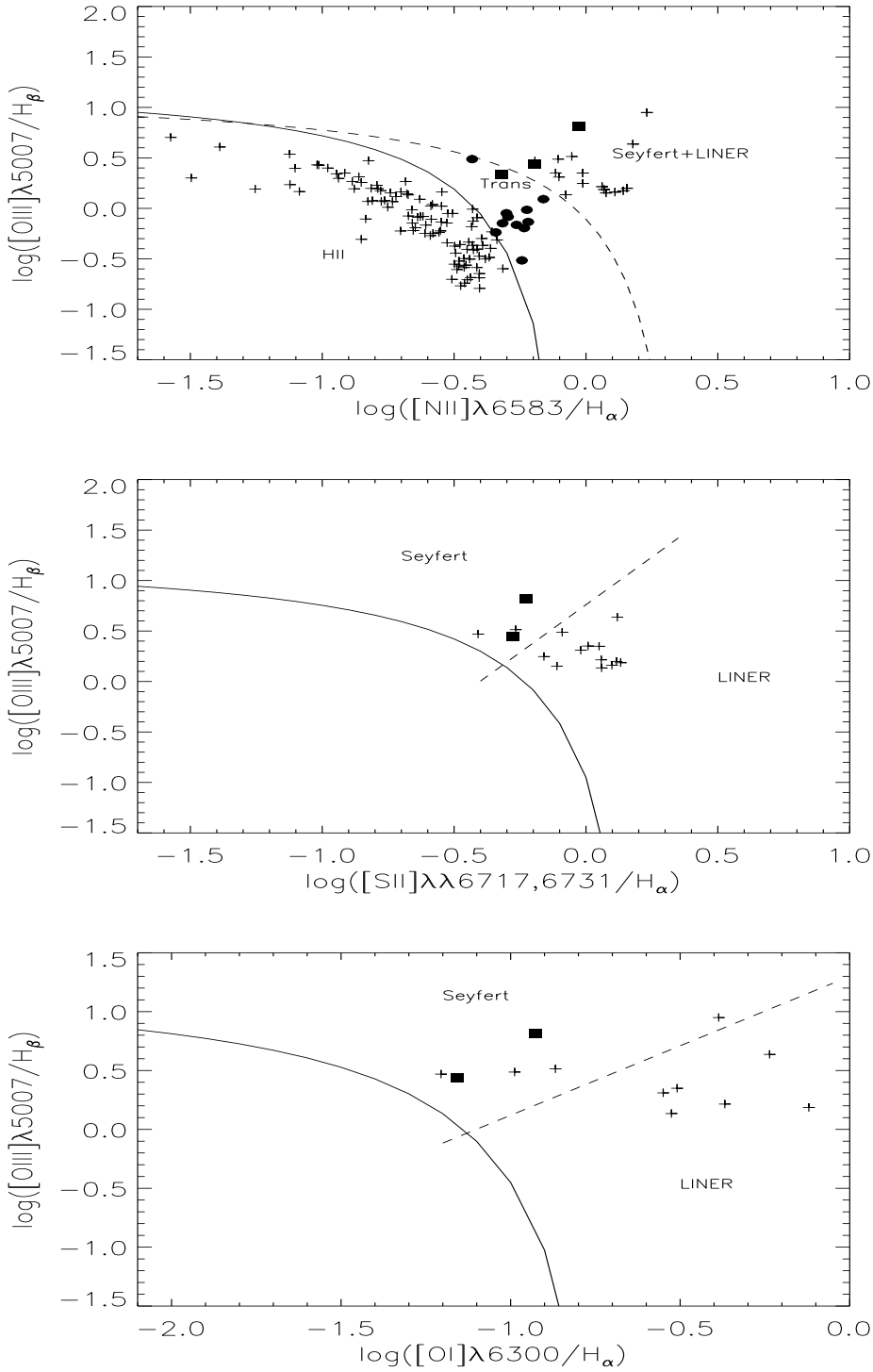


Fig. 5.— The emission line diagnostic diagram based on the AGN classification scheme of Ke06 for 131 emission-line LSBGs with the $\text{H}\beta$, $[\text{OIII}]\lambda 5007$, $\text{H}\alpha$ and $[\text{NII}]\lambda 6583$ four lines detected with $\text{S/N} > 3$. The dashed curve in top panel shows the demarcation between starburst galaxies and AGNs defined by Ke01. While the solid curve shows the revised demarcation given in Ka03. The filled circle in the top panel represents composite object. The solid curves in middle and bottom panels represent the demarcation between starburst galaxies and AGNs defined by Ke01, and the dashed lines represent the demarcation between Seyfert galaxies and LINERs. Broad line AGN is

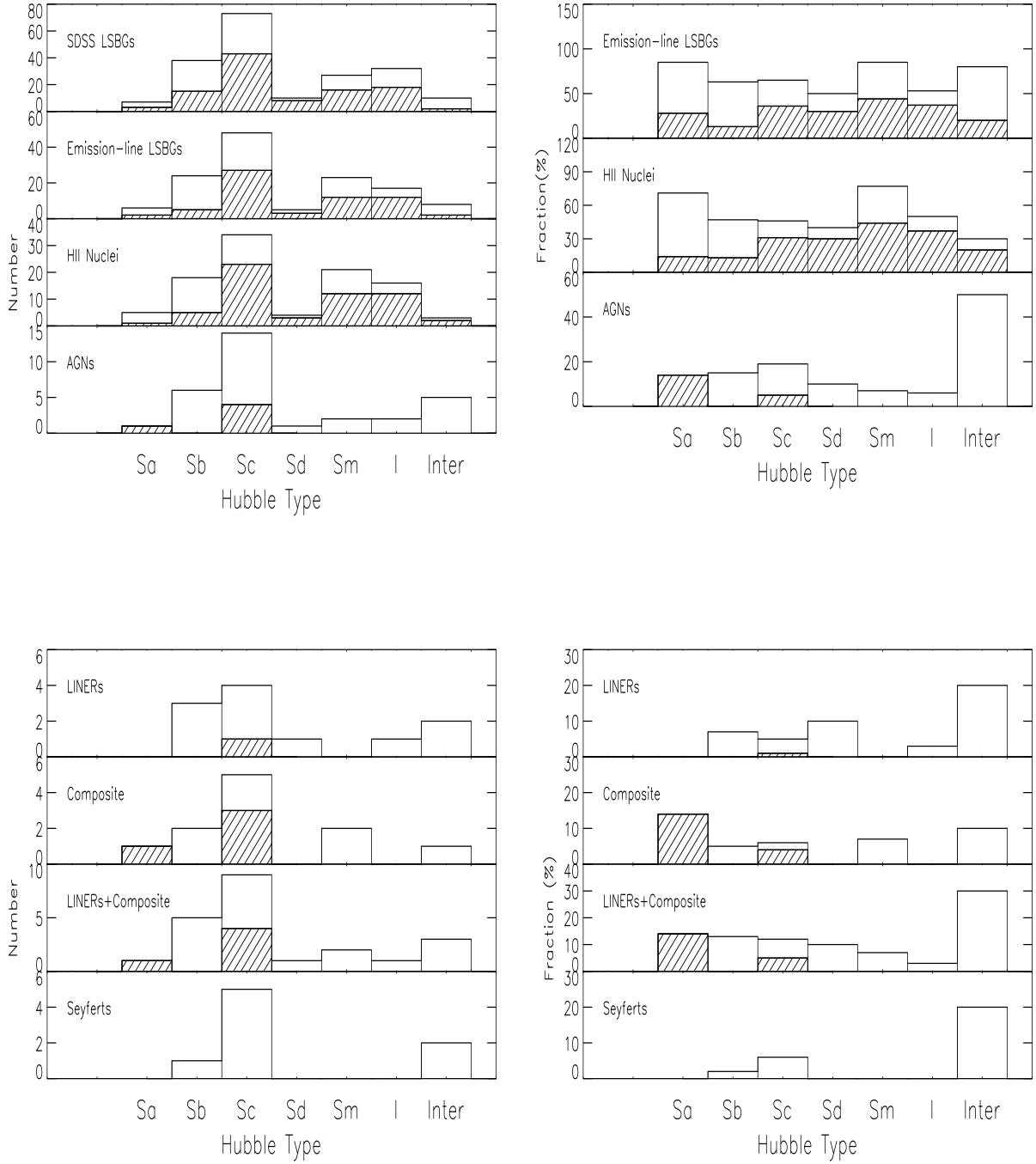


Fig. 6.— Number statistics and detection rates of LSBGs as a function of morphological types of all emission-line nuclei, HII nuclei, and AGNs. LSBGs with $\mu_0^B \geq 22.0 \text{ mag arcsec}^{-2}$ are shown by hatched histogram.

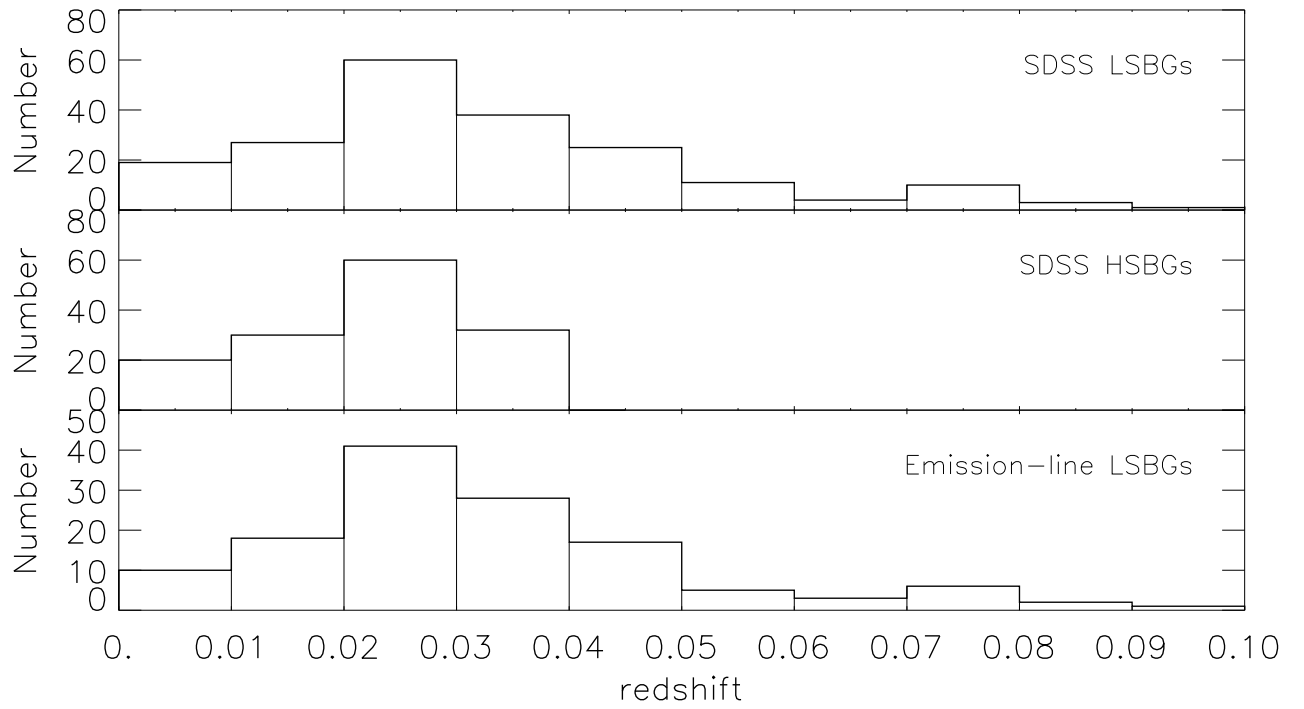


Fig. 7.— Distribution of redshift for the APM-SDSS LSBGs (top panel), the comparing HSBG sample (middle panel) and the 131 emission-line LSBGs (bottom panel).

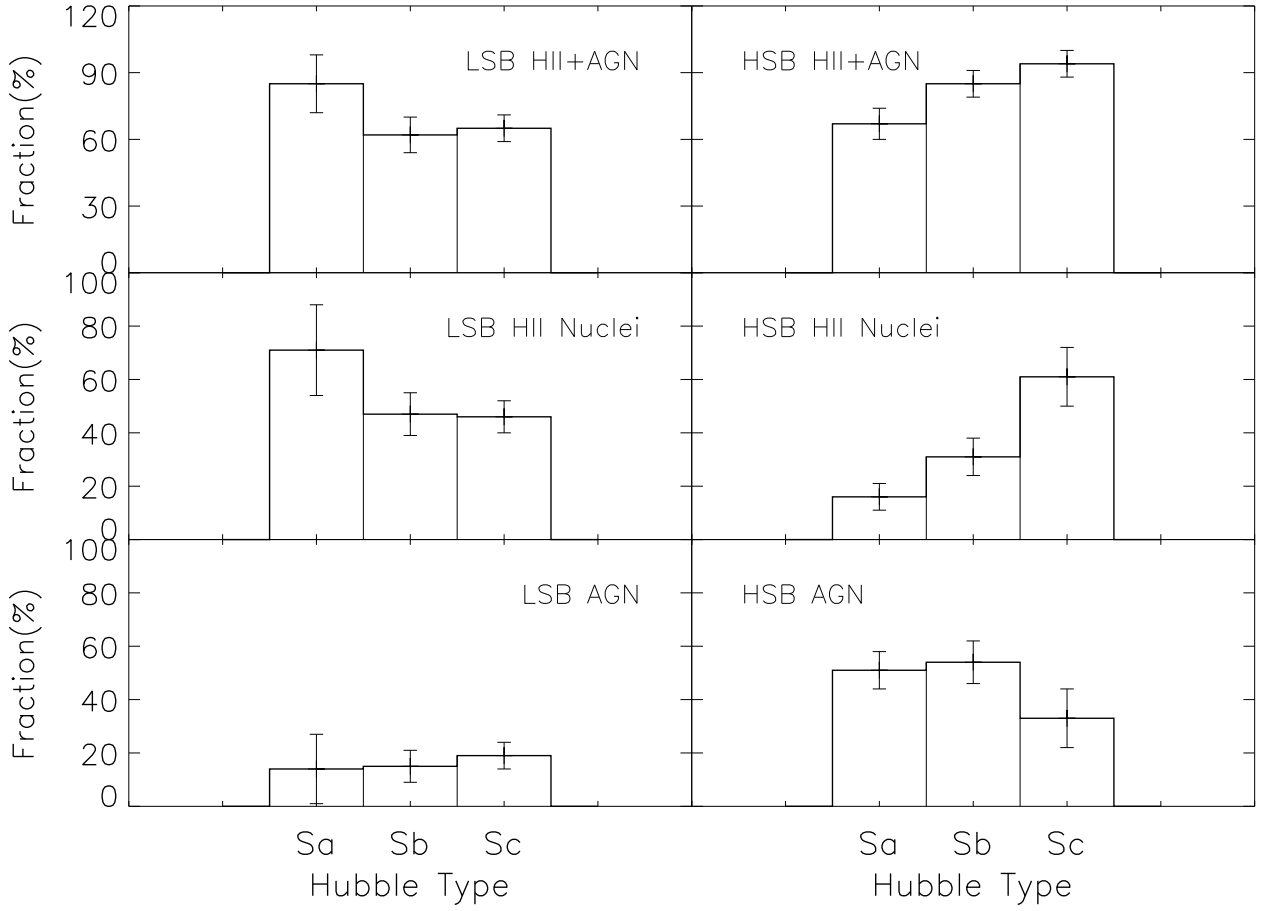


Fig. 8.— Fraction of galaxies containing star-forming and AGN nuclei for the LSBGs with $z < 0.04$ (left panels) and the comparing HSBG sample (right panels), for the Sa, Sb and Sc types.

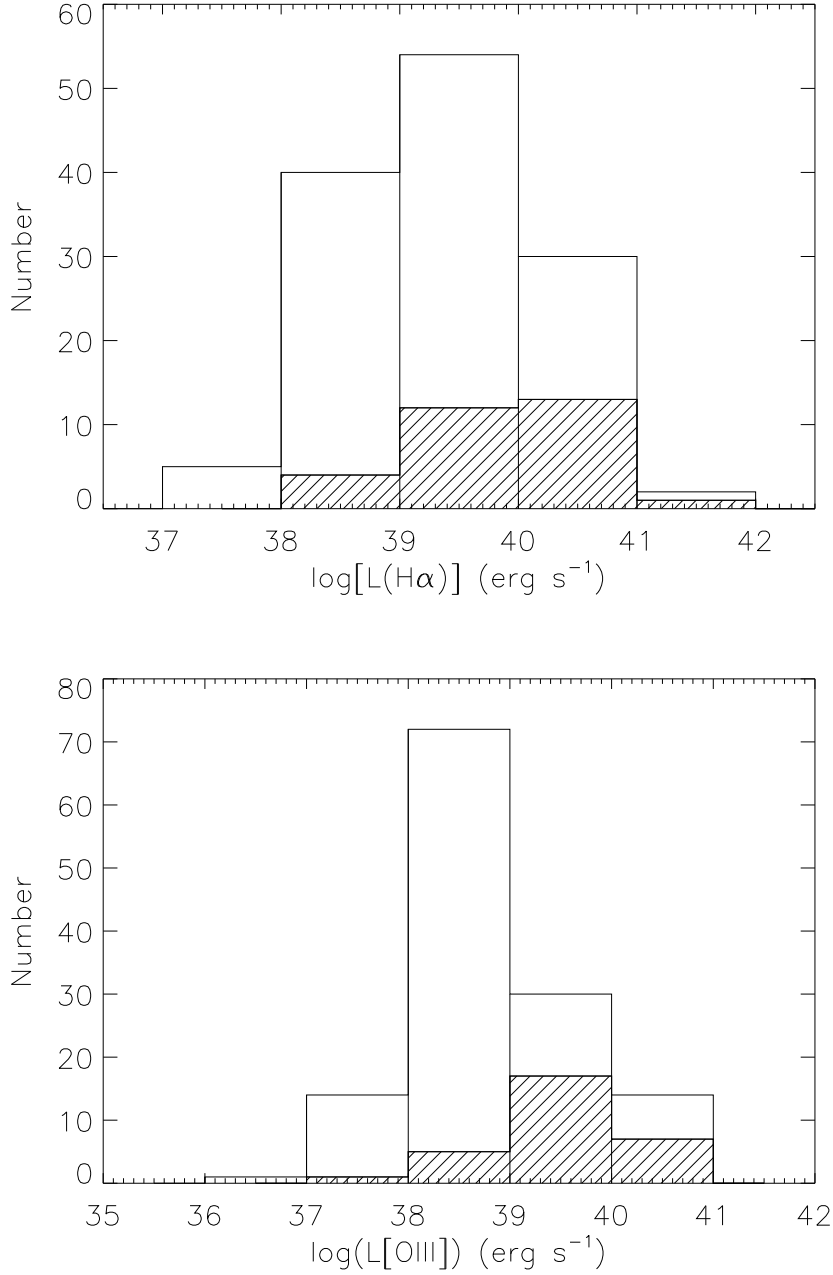


Fig. 9.— Distributions of luminosities of the narrow H α line (in units of erg s $^{-1}$) and [OIII] λ 5007 line of LSBGs. That the higher [OIII] λ 5007 luminosities, the higher fractional AGNs indicates that [OIII] λ 5007 luminosities are correlated with the strength of AGN activities. The hatched histogram denotes AGNs.

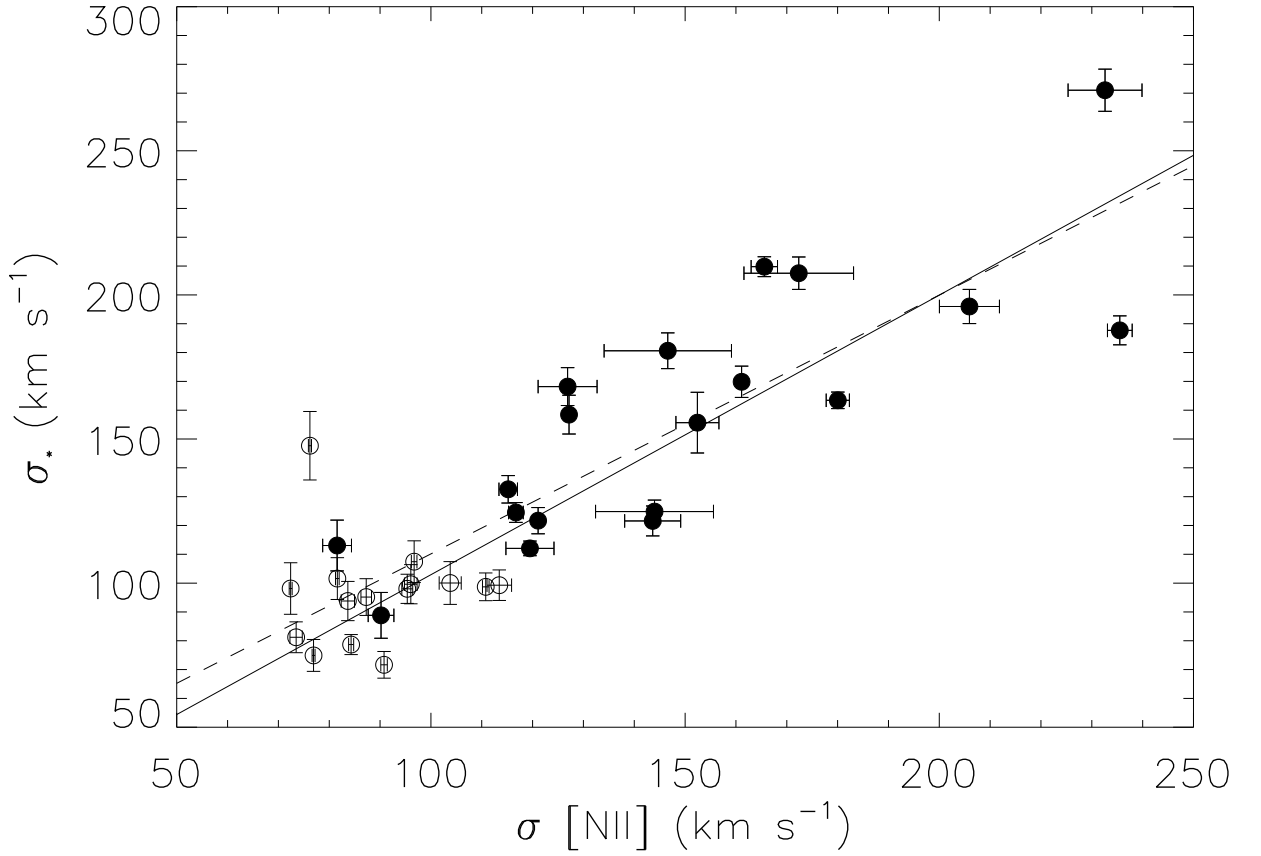


Fig. 10.— Relationship between the width of the [NII] emission line and the galactic stellar velocity dispersion σ_* for 34 LSBGs which have both measurements of σ [NII] and σ_* with S/N > 5, including 19 AGNs (filled-circles) and 15 star-forming galaxies (open circles). Also plotted are linear relations for all the 34 LSBGs (solid line) and for AGNs only (dashed line) fitted by the regression analysis taking into account the errors in both the variables.

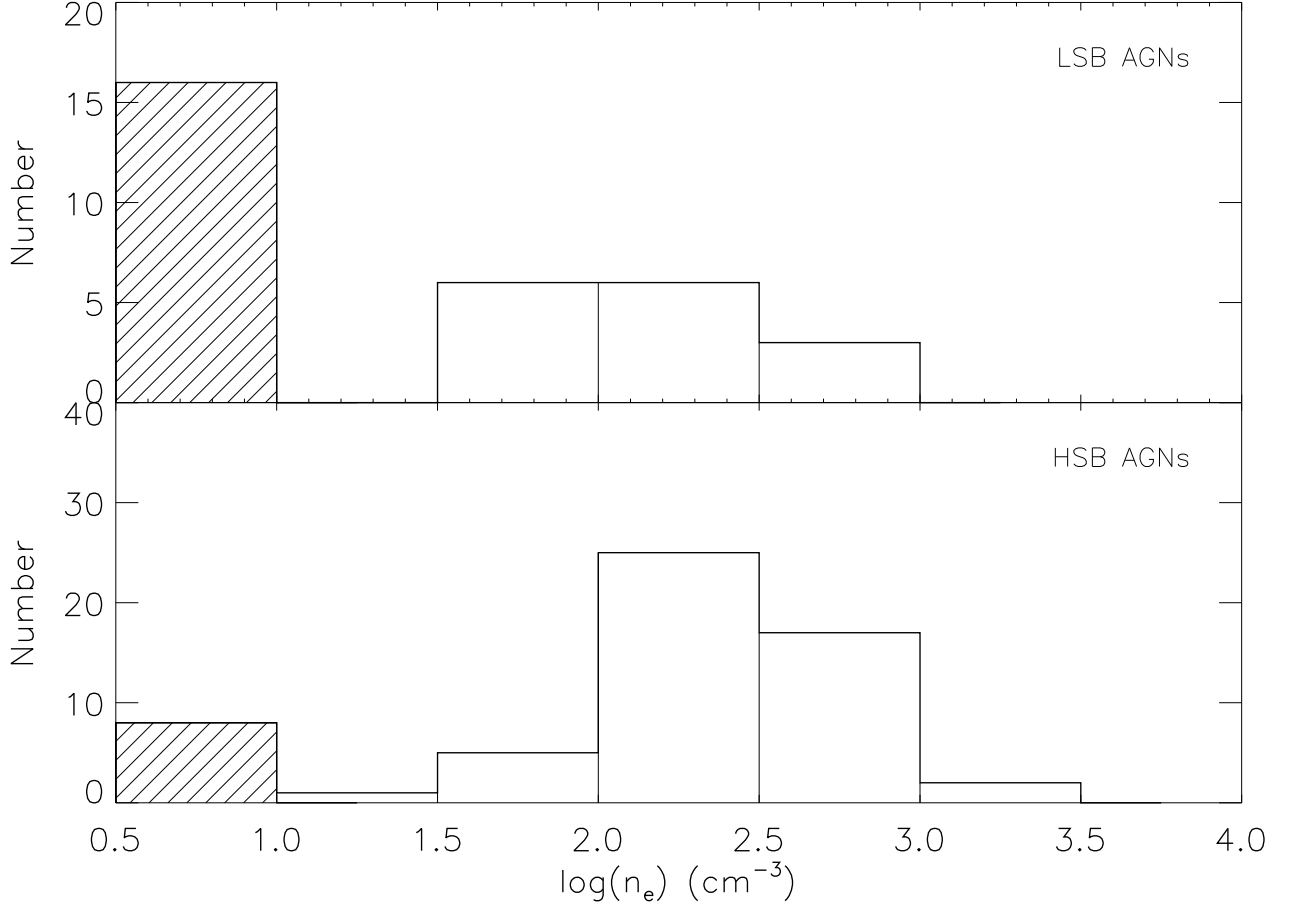


Fig. 11.— Distribution of the narrow–line region (NLR) electron densities of AGNs in LSBGs (upper panel) and in the comparing sample of HSBGs (lower panel). An upper limit of $n_e = 10 \text{ cm}^{-3}$ is set to those with $F_{[SII]\lambda 6717} / F_{[SII]\lambda 6731}$ greater than 1.42, which are shown as hatched histogram. AGNs in LSBGs tend to have lower NLR electron densities than those of HSBGs (the probability that the two samples have the same distribution is $P_{ks} = 7.0 \times 10^{-5}$).

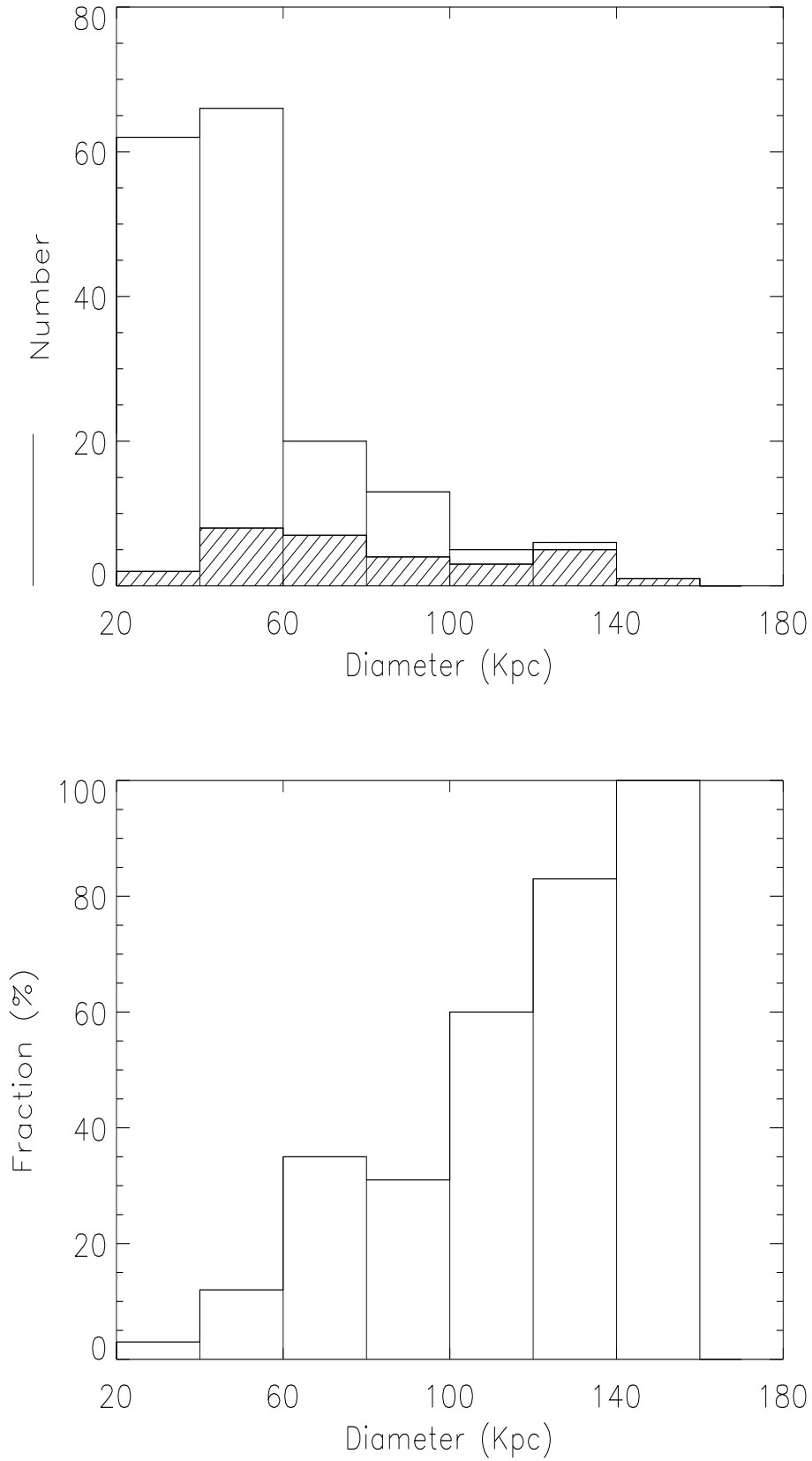


Fig. 12.— Distribution of the physical sizes of LSBGs (upper panel, AGNs are plotted as hatched

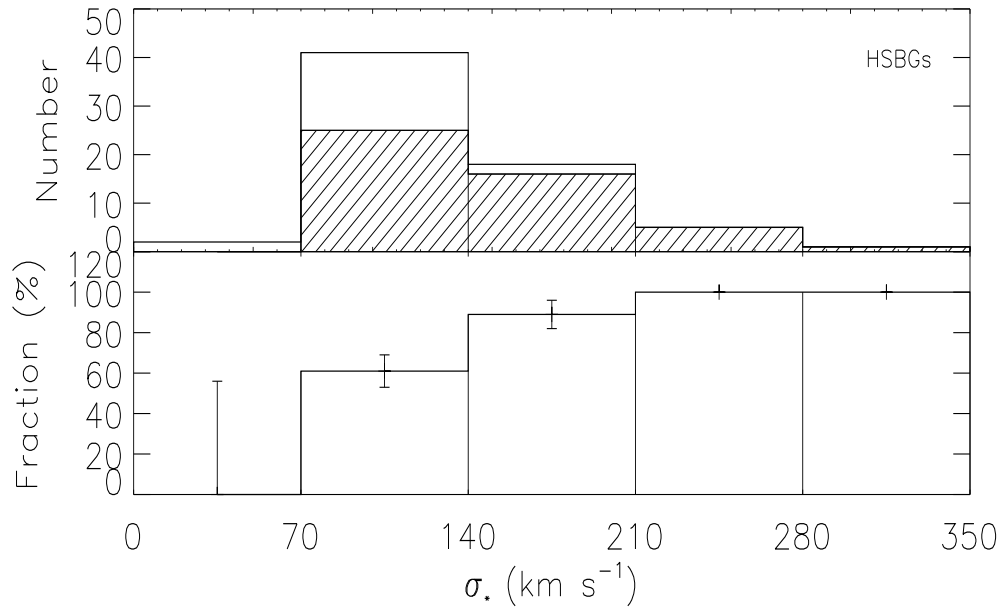
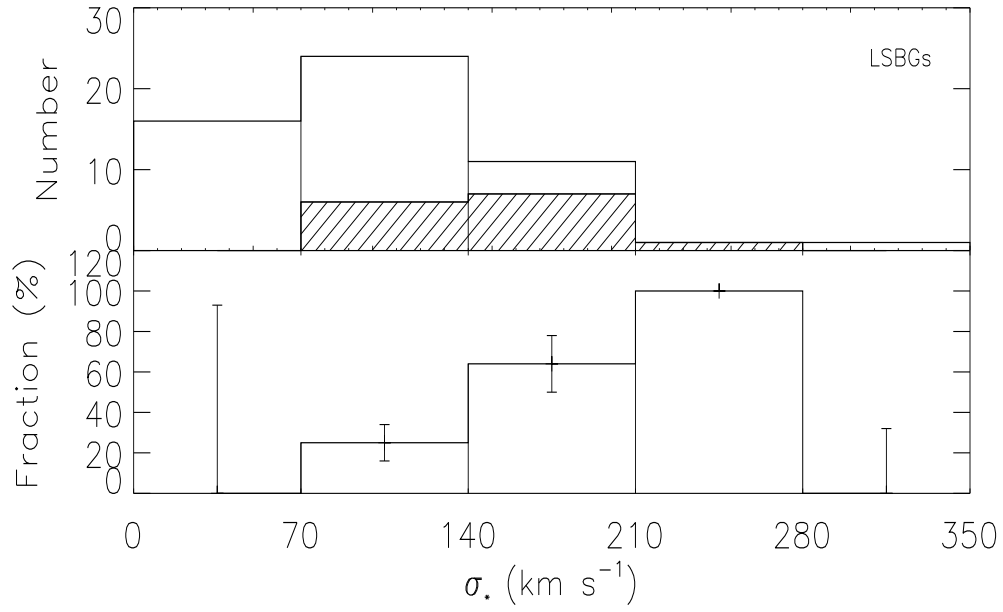


Fig. 13.— Distributions of emission-line galaxies (top panel) and the AGN fraction (bottom panel)

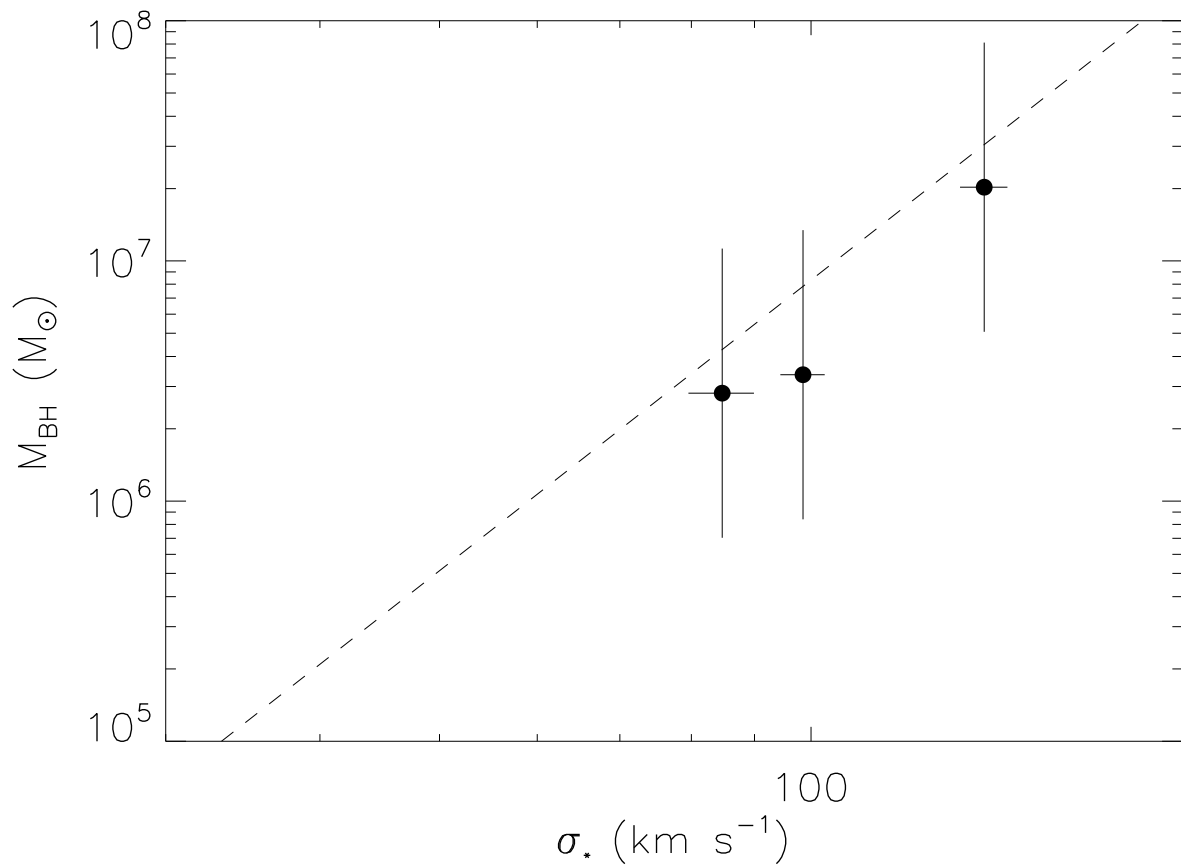


Fig. 14.— Relation between the stellar velocity dispersion and the black hole mass for 3 broad line AGNs in LSBGs. The black hole masses are uncertain by a factor of 4. The dashed line is the relation given by Tremaine et al. (2002) for local normal galaxies and AGNs.

